



**HAL**  
open science

# Surface Conditioning Effects on Submerged Optical Sensors: A Comparative Study of Fused Silica, Titanium Dioxide, Aluminum Oxide, and Parylene C

Zibin Nan, Pascal Floquet, Didier Combes, Claire Tendero, Mickaël Castelain

## ► To cite this version:

Zibin Nan, Pascal Floquet, Didier Combes, Claire Tendero, Mickaël Castelain. Surface Conditioning Effects on Submerged Optical Sensors: A Comparative Study of Fused Silica, Titanium Dioxide, Aluminum Oxide, and Parylene C. *Sensors*, 2023, 23 (23), pp.9546. 10.3390/S23239546 . hal-04350817

**HAL Id: hal-04350817**

**<https://cnrs.hal.science/hal-04350817>**

Submitted on 26 Mar 2024

**HAL** is a multi-disciplinary open access archive for the deposit and dissemination of scientific research documents, whether they are published or not. The documents may come from teaching and research institutions in France or abroad, or from public or private research centers.

L'archive ouverte pluridisciplinaire **HAL**, est destinée au dépôt et à la diffusion de documents scientifiques de niveau recherche, publiés ou non, émanant des établissements d'enseignement et de recherche français ou étrangers, des laboratoires publics ou privés.

## Article

# Surface Conditioning Effects on Submerged Optical Sensors: A Comparative Study of Fused Silica, Titanium Dioxide, Aluminum Oxide, and Parylene C

Zibin Nan <sup>1</sup>, Pascal Floquet <sup>2</sup>, Didier Combes <sup>1</sup>, Claire Tendero <sup>3</sup> and Mickaël Castelain <sup>1,\*</sup>

<sup>1</sup> TBI, Université de Toulouse, CNRS UMR5504, INRAe UMR792—INSA 135, avenue de Rangueil, 31055 Toulouse, France

<sup>2</sup> LGC, Université de Toulouse, CNRS, INPT, UPS—ENSIACET 4, allée Émile Monso, 31030 Toulouse, France; pascal.floquet@toulouse-inp.fr

<sup>3</sup> CIRIMAT, Université de Toulouse, CNRS, INPT, UPS—ENSIACET 4, allée Émile Monso, 31030 Toulouse, France; claire.tendero@inp-toulouse.fr

\* Correspondence: mickael.castelain@insa-toulouse.fr

**Abstract:** Optical sensors excel in performance but face efficacy challenges when submerged due to potential surface colonization, leading to signal deviation. This necessitates robust solutions for sustained accuracy. Protein and microorganism adsorption on solid surfaces is crucial in anti-biofilm studies, contributing to conditioning film and biofilm formation. Most studies focus on surface characteristics (hydrophilicity, roughness, charge, and composition) individually for their adhesion impact. In this work, we tested four materials: silica, titanium dioxide, aluminum oxide, and parylene C. Bovine Serum Albumin (BSA) served as the biofouling conditioning model, assessed with X-ray photoelectron spectroscopy (XPS). Its effect on microorganism adhesion (modeled with functionalized microbeads) was quantified using a shear stress flow chamber. Surface features and adhesion properties were correlated via Principal Component Analysis (PCA). Protein adsorption is influenced by nanoscale roughness, hydrophilicity, and likely correlated with superficial electron distribution and bond nature. Conditioning films alter the surface interaction with microbeads, affecting hydrophilicity and local charge distribution. Silica shows a significant increase in microbead adhesion, while parylene C exhibits a moderate increase, and titanium dioxide shows reduced adhesion. Alumina demonstrates notable stability, with the conditioning film minimally impacting adhesion, which remains low.

**Keywords:** serum protein adsorption; polystyrene microbeads adhesion; shear stress flow chamber; principal component analysis; X-ray photoelectron spectroscopy



**Citation:** Nan, Z.; Floquet, P.; Combes, D.; Tendero, T.; Castelain, M. Surface Conditioning Effects on Submerged Optical Sensors: A Comparative Study of Fused Silica, Titanium Dioxide, Aluminum Oxide, and Parylene C. *Sensors* **2023**, *23*, 9546. <https://doi.org/10.3390/s23239546>

Academic Editor: Stephen Holler

Received: 25 October 2023

Revised: 17 November 2023

Accepted: 27 November 2023

Published: 30 November 2023



**Copyright:** © 2023 by the authors. Licensee MDPI, Basel, Switzerland. This article is an open access article distributed under the terms and conditions of the Creative Commons Attribution (CC BY) license (<https://creativecommons.org/licenses/by/4.0/>).

## 1. Introduction

Optical sensors, renowned for their exceptional performance, face potential efficacy challenges when submerged due to the susceptibility of the outer surface to biological colonization [1–3]. This colonization, in turn, can lead to signal deviation, necessitating the development of robust solutions to ensure sustained accuracy and functionality. The protection of environmental sensors [2] is an important issue in so far as such sensors have to operate continuously and autonomously in immersion during several months (at least around 3 months) to collect high quality data. While immersed they undergo aggressions such as biofouling; i.e., microbial adhesion and biofilm formation, and therefore they have to be protected. Biofouling, denoting the colonization of microorganisms or macroorganisms on solid surfaces within aqueous environments [4], transitions into a biofilm during the stage of microorganism adhesion. A biofilm constitutes a structured community of bacterial populations enclosed in a self-produced polymeric matrix, firmly adhering to an inert or living surface [5,6]. The prevalence of biofouling and biofilm formation raises significant

concerns across various domains, notably in marine sectors [7], food industries [8], medical contexts [9,10], and environmental monitoring [11,12]. Consequently, a substantial body of research has been dedicated to exploring antifouling strategies in recent decades, with a pronounced focus on environmentally sustainable alternatives following the prohibition of tributyltin compound applications in antifouling coatings in 2003 [13–15]. Most identified or strategies under research focus on prevention or denaturation of biofilm in the early stage of formation, mainly by avoiding the adhesion of particles or cells from the environment on the studied surface. These strategies include the application of nanomaterials, which benefits from their physical properties, such as silver nanoparticle [16,17], titanium dioxide (TiO<sub>2</sub>) [18–23], and zinc oxide [24–29], the modification of surface with protein-resistant polymers [30–32], or slippery liquid-infused porous method [33] or self-assembled monolayers, which is able to control the adhesion through steric repulsion [34–38] and the immobilization of hydrolytic enzymes on the studied surface [39–43]. Despite the effectiveness of certain strategies, limited research has provided comprehensive elucidation of the molecular and physical interactions occurring during the adhesion process. As delineated in the existing literature, the mechanism of adhesion interaction is predominantly influenced by foundational determinants [44], including surface hydrophobicity/hydrophilicity [45–49], surface roughness [49–51], surface charge [45,52,53], chemical composition of the surface or adsorbate, such as functional groups [46,54], and the electrolytic environment [55–57]. In a general sense, the phenomenon of microbial adhesion is typically preceded by the establishment of a conditioning film [58–60] comprising macromolecular constituents. Through the adsorption of organic particles, conditioning films form on the substrate surface, potentially modifying the surface properties and thereby facilitating microbial adhesion [59,61–63]. The constituents of these conditioning films can vary significantly based on the environmental context to which the surface is exposed, thereby influencing the adhesion behavior of microorganisms, either augmenting or attenuating it [62–64].

In the context of environmental observatory and the imperative to devise novel strategies for mitigating biofouling on autonomous optical sensors deployed in continental waters, this study is dedicated to probing the nexus between physicochemical properties of coated or nanostructured surfaces and their propensity for adhesion of calibrated solid particles. Furthermore, the investigation extends to scenarios involving the presence of model conditioning proteins. The main goal is to propose some anti-fouling surfaces to prevent the adsorption of protein and provide a link to subsequent initial adhesion of particles.

To address this inquiry, four distinct specimens (namely fused silica, titanium dioxide, alumina, and parylene C) were subject to comprehensive characterization encompassing roughness, surface zeta potential, hydrophilicity, and surface chemical composition. For the sake of methodological simplicity, models were employed to emulate conditioning films, exemplified by Bovine Serum Albumin (BSA), as well as microorganisms represented by functionalized hydrophobic polystyrene microbeads. Subsequently, the detachment profiles of charged microbeads—denoting the count of adhered particles capable of withstanding shear flow relative to the applied shear stress—were assessed utilizing shear stress flow technique. These evaluations were conducted on both unaltered specimens and those subjected to BSA conditioning. Ultimately, the correlation among these findings was scrutinized through Principal Component Analysis (PCA).

## 2. Materials and Methods

### 2.1. Materials

To guarantee the best signal on immersed optical sensors, fused silica is a widely used material as the interface between the sensor and the environmental medium. Fused silica (f-SiO<sub>2</sub>) raw samples, NEGS1 quality, dimensioned for flow chamber (30 × 9 × 0.9 mm<sup>3</sup>) and for zeta potential (29.9 × 19.9 × 0.35 mm<sup>3</sup>) measurements, were purchased from Neyco and BSA purchased from Sigma Aldrich (Sigma-Aldrich Chimie, Saint-Quentin-Fallavier, France). Functionalized polystyrene microbeads were purchased from Spherotech (Spherotech, Inc., Lake Forest, IL, USA). Two functions were chosen, amine groups NH<sub>2</sub> (6.2 ± 0.8 μm in diame-

ter) and carboxyl groups COOH ( $6.8 \pm 0.7 \mu\text{m}$  in diameter). The diameters of the microbeads were measured using Malvern Mastersizer 3000 (Malvern Panalytical, Palaiseau, France) and fit to the specifications of the manufacturer. The suspending medium was Evian™ (Danone, Rueil-Malmaison, France) water purchased from the supermarket. Evian™ water has shown very similar physico-chemical properties as continental water in terms of ionic strength and pH, and the same batch was tested throughout the experiments presented in this paper. The electrical conductivity and pH was measured at  $23 \text{ }^\circ\text{C}$  as  $\sigma = 534 \pm 30 \mu\text{S}\cdot\text{cm}^{-1}$  and  $\text{pH} = 7.2 \pm 0.1$ , respectively. The total amount of dissolved solids was provided by the manufacturer at  $345 \text{ mg/L}$ . Ionic strength is approximated to  $I = 9.1 \pm 0.5 \text{ mM}$ . These values fit the drinkable water standards and to the majority of superficial natural waters in France (for instance, a real-time monitoring database, as in Ref. [65]).

## 2.2. Preparation of Samples

Titanium dioxide ( $\text{TiO}_2$ , anatase as crystalline structure), Aluminum oxide ( $\text{Al}_2\text{O}_3$ , amorphous), and Parylene C ( $\text{C}_8\text{H}_7\text{Cl}$ )<sub>n</sub> coatings were deposited on fused silica by chemical vapor deposition. The depositions are presented in Table 1. Further details can be found in the referenced works. Before deposition process and further characterizations, fused silica samples were cleaned with ethanol, then rinsed in deionized water and dried under argon flow at room temperature.

**Table 1.** Process parameters for the deposition of coatings, where  $d$  is the coating thickness,  $P$  and  $T$  are the operating pressure and temperature for deposition, respectively.

Coating	Precursor	Deposition Parameters	Reference
$\text{TiO}_2$ $d \sim 300\text{--}400 \text{ nm}$	Titanium isopropoxide Bubbling at $50 \text{ }^\circ\text{C}$ under nitrogen flow	$P = 5 \text{ mbar}$ $T = 400 \text{ }^\circ\text{C}$	[66]
$\text{Al}_2\text{O}_3$ $d \sim 300 \text{ nm}$	Aluminium isopropoxide Direct liquid injection	$P = 5 \text{ mbar}$ $T = 500 \text{ }^\circ\text{C}$	[67]
Parylene C $d \sim 300 \text{ nm}$	dichloro[2,2]paracyclophane Sublimation at $140 \text{ }^\circ\text{C}$ then pyrolysis at $670 \text{ }^\circ\text{C}$	$P = 10^{-2} \text{ mbar}$ $T \text{ room temperature}$	[68]

## 2.3. Conditioning Film

BSA was chosen as the model protein to form the conditioning film on surface. BSA solution was prepared with a concentration of  $1 \text{ g/L}$  in Evian™ water to model the ionic strength of real immersion media. In Evian™ water, the ionic strength is  $6.3 \text{ mM}$ . Samples were immersed in BSA solution for  $4 \text{ h}$  to favor protein adsorption, and were then left dehydrating at room temperature under laminar flow hood, atmospheric pressure, and room temperature.

## 2.4. Polystyrene Microbeads

In order to understand the influence of coatings, polystyrene microbeads functionalized with carboxyl group ( $-\text{COOH}$ ) or amino group ( $-\text{NH}_2$ ) have been chosen as the model of microorganism due to their similar size to microorganisms such as yeast cells or microalgae ( $5 \text{ to } 7 \mu\text{m}$  in diameter) [69], their controllable density and non-pathogenic character. Moreover, carboxyl and amino groups are fundamental functional groups in protein and carry negative and positive charge, respectively: therefore, they can also be useful for assessing the protein adsorption mechanism. A volume of  $100 \mu\text{L}$  original stock polystyrene microbeads was dispersed in  $900 \mu\text{L}$  Evian™ water and vortexed, then centrifuged at  $13,000 \text{ rpm}$  for  $6 \text{ min}$ . The precipitate was dissolved in  $1 \text{ mL}$  Evian™ water and sonicated before use.

### 2.5. Atomic Force Microscopy (AFM)

The surface topography and roughness of bare surface samples were analyzed using an atomic force microscope (AFM, Agilent 5500<sup>TM</sup>, SCIENTEC, Les Ulis, France), in tapping mode with regular Si (N-type) tips that have the following physical characteristics: curvature lower than 10 nm, stiffness between 25 and 75 N/m and resonance frequency in the 200–400 kHz range. Quadratic roughness calculation result from the analyses of  $2 \times 10$  images (scanned area:  $1 \mu\text{m}^2$ ) recorded on two specimens of each surface.

### 2.6. Water Contact Angle

The water contact angle of samples was investigated using Evian<sup>TM</sup> water as sessile droplet via goniometer (DigiDrop<sup>TM</sup>, GBX, Romans-sur-Isère, France) on both bare and BSA-conditioned samples. For each surface, 10 measurements were performed, and each surface was triplicated. The conditioned samples were preliminarily immersed in BSA solution during 4 h.

### 2.7. Surface Charge

The surface charge of carboxyl group and amino group functionalized polystyrene microbeads and BSA molecule in the concentration of 1 g/L, were measured in 1 mM KNO<sub>3</sub> solution using Zetasizer nano series (Malvern Instruments, Saclay, France). Zeta potential  $\zeta$  of the flat samples surface ( $19.9 \times 29.9 \times 0.35 \text{ mm}^3$ ) was measured with ZetaCAD<sup>®</sup> setup (CAD Instruments, Les Essarts Le Roi, France). A volume of 1-mM KNO<sub>3</sub> electrolyte solution was forced to pass through a capillary that consists of 2 similar flat samples separated by 200  $\mu\text{m}$ -thick polytetrafluoroethylene spacers. The excess charges around the surface are carried along by the electrolyte. Their accumulation downstream results in an electric field that drives an electric current back by ionic conduction, through the liquid, against the direction of the liquid flow. A steady state is quickly established and the potential difference (between upstream and downstream) is measured with silver electrodes: this potential difference is called the streaming potential  $\Delta E$  [70–72]. This streaming potential is linked to the zeta potential  $\zeta$  (Equation (1)) through the Helmholtz–Smoluchowski approximation [73] that takes into account the physicochemical characteristics of the measurement medium:

$$\frac{\Delta E}{\Delta P} = \frac{\epsilon_0 \epsilon_r \zeta}{\mu \chi}, \quad (1)$$

where  $\Delta P$  is the charge loss in the streaming channel (Pa),  $\Delta E$  the streaming potential (V),  $\epsilon_0$  the vacuum permittivity ( $\text{F}\cdot\text{m}^{-1}$ ),  $\epsilon_r$  the solvent relative dielectric constant relative,  $\zeta$  the zeta potential (V),  $\mu$  the dynamic viscosity of electrolyte solution ( $\text{Pa}\cdot\text{s}$ ), and  $\chi$  the conductivity of electrolyte solution ( $\text{S}\cdot\text{m}^{-1}$ ). Before measurement, the samples were immersed in the electrolyte for 1 h for stabilization. In the case of BSA conditioning, samples were first immersed for 4 h in the BSA solution. The zeta potential was measured on both bare and BSA-conditioned surfaces. Each measurement was triplicated.

### 2.8. X-ray Photoelectron Spectroscopy (XPS)

Surface chemical composition was analyzed on both bare and conditioned substrates by performing X-ray photoelectron spectroscopy (XPS) measurements with a spectrometer (Thermo Scientific<sup>TM</sup> Kalpha<sup>TM</sup>, Thermo Electron SAS, Toulouse, France) equipped with a monochromatic anticathode Al ( $K\alpha$  radiation of 1486.7 eV), under less than  $5 \times 10^{-9}$  mbar pressure. The energy calibration was performed using Au4f<sub>7/2</sub> ( $83.9 \pm 0.1$  eV) and Cu2p<sub>3/2</sub> ( $932.7 \pm 0.1$  eV) photoelectron lines. Charging compensation and neutralization was applied using a dual beam flood gun. The diameter of probed area was  $\sim 400 \mu\text{m}$ . Each surface was characterized with two spots and duplicated. High-resolution spectra fitting was performed using NIST (<https://srdata.nist.gov/xps/>, accessed on 15 January 2023) database [74]. Conditioned samples were immersed in BSA solution, then rinsed with Evian<sup>TM</sup> water and dried with Argon whereas the bare substrates were only immersed in Evian<sup>TM</sup> and dried with Argon. The comparison allows the investigation on BSA

adsorption separated from the contribution of the immersion in water. As XPS analyses the extreme surface (the first 10 nm), the immersion time in BSA solution or Evian™ water was set to 10 min in order to characterize the earliest steps of BSA adsorption and highlight the potential differences between the various surface behaviors and adsorption kinetics. Additionally, a 24-h immersion was tested in order to enhance the trends revealed during the first 10 min and favor the conditioning film formation in the case of very low adsorption kinetics.

### 2.9. Shear-Stress Flow Chamber

Shear flow-induced detachment experiments were performed to measure the adhesion of microorganisms on surfaces [55,75] or model particles [45,69] using a dedicated setup [45]. Polystyrene microbeads were selected as models of microorganisms. The flow chamber consisted of a rectangular channel of a very small cross section in which the flow could be kept laminar. The wall shear stress,  $\tau_w$  (Pa), was thus perfectly controlled and it was assumed to be uniform over the whole coupon, i.e., the substrate surface. The previously described experimental procedure [75] was slightly modified, notably for the cell-counting mode. In brief, shear-flow induced microbeads detachment was analyzed in a rectangular flow channel (9 mm width, 30 mm length, and 200  $\mu\text{m}$  thickness). The wall shear stress  $\tau_w$  can be expressed as follows:

$$\tau_w = \frac{3\mu Q}{4h^2l}, \quad (2)$$

where  $Q$  is the volumetric flow rate ( $\text{m}^3/\text{s}$ ),  $\mu$  is the dynamic viscosity (Pa.s),  $h$  is the channel half height (m), and  $l$  is the channel half width (m). An upright optical microscope (Nikon Eclipse LV100, Nikon Europe B.V., Amstelveen The Netherlands) equipped with a 20 $\times$  working distance objective was set to observe experiments under the reflection mode, and a camera (digital STGHT DS-2MBW, Nikon Europe B.V., Amstelveen The Netherlands) with the NIS-Elements F3.0 video acquisition software was applied to record the image. Before starting the experiment, the flow chamber and all tubes were fulfilled with Evian™, while all air bubbles were removed thoroughly from the system. The microbead suspension (with a volume of 1 ml at about  $10^6$  particles/mL) was slowly injected into the flow chamber and then the beads could settle and attach to the substrate surface for 30 min under static condition. The initial number of adhered microbeads was recorded as  $N_0$ . A laminar flow was then imposed, with a stepwise increased flow rate ranging the corresponding wall shear stress  $\tau_w$  from 0 to 80 Pa. At the end of each step, the number of microbeads remaining adherent to the surface ( $N$ ) was counted. The detachment profile ( $N/N_0 = f(\tau_w)$ ) was then plotted (not shown). Experiments were performed in duplicate both on bare and BSA-conditioned samples (after 4 h immersion).

### 2.10. Principal Component Analysis

Principal component analysis (PCA) is a statistical tool that is used to reduce the dimensionality of large datasets, by transforming the set of variables into a smaller one that still contains most of the information in the large set ([76]). It reveals the correlations between variables and provides efficient plots that facilitate the interpretation. Datasets (individuals or variables) are represented in a new coordinate system consisting of 'principal components' (PCs), i.e., the axes of variability of the initial scatter graph. The raw data is converted into a standardized set of data by using the mean value and standard deviation. These standardized data are then compared with each other, leading to a correlation matrix. The matrix diagonalization results in a new set of coordinates named as *principal components*. Those principal components lead to different types of information:

- **Score plot:** The samples are plotted as a function of the new coordinate system and it can help to group samples with similar characteristics.  $\text{Cos}^2\theta$  calculated from the coordinates of the samples gives information on the quality of the sample description in the reduced space and thus the reliability of the drawn conclusion: the closer  $\text{cos}^2\theta$  is to one, the better the description;

- **Loading plot:** The variables are plotted as a function of the principal coordinates. Usually, two or three PCs are sufficient to take into account a large part of the data variability. Vectors that represent each variable should be drawn from the center: if there is, approximately, a  $\sim 90^\circ$  difference between the vectors, then the two variables are not correlated, while a difference of  $\sim 180^\circ$  means that the two variables are anti-correlated and if the angle is small (approximately  $\sim 0^\circ$ – $30^\circ$ ) between the two vectors then they are strongly related.

### 3. Results

#### 3.1. Roughness and Topography

AFM technique was used to map out the surface topography and evaluate the quadratic roughness of the four investigated materials as presented on Figure 1. Fused silica is the flattest one with a 0.7 nm average roughness. Titanium dioxide exhibited the roughest topography on a nanoscale level, about 20 times higher than fused silica. The quadratic roughness of aluminum oxide and parylene C was between fused silica and titanium dioxide, respectively, being twice and three times higher than fused silica.

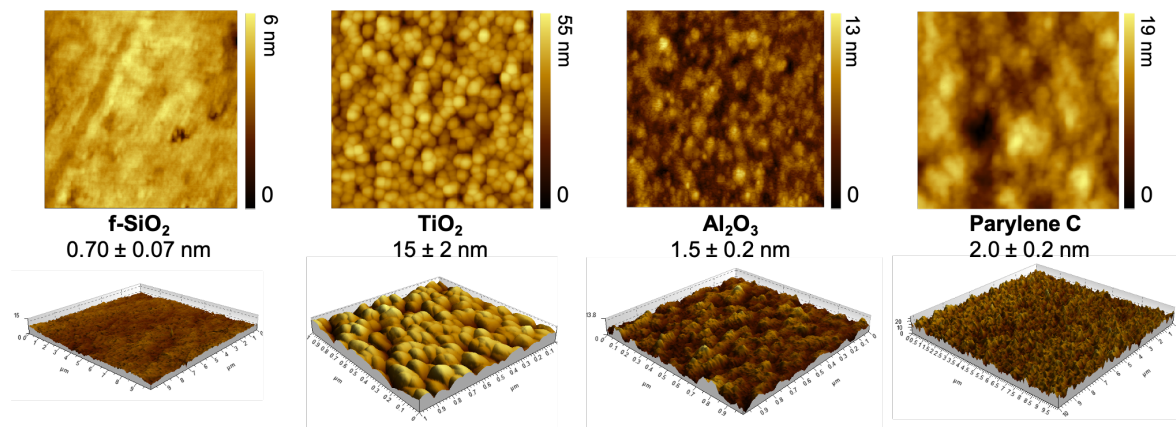


**Figure 1.** AFM mapping of surface topography within a  $1\text{-}\mu\text{m}^2$  area and measurement of quadratic roughness (nm).

#### 3.2. Hydrophobicity

Figure 2A displays the water contact angle on these various surfaces, bare and after immersion in the BSA solution. Titanium dioxide showed a high hydrophilicity, whereas aluminum oxide and parylene C demonstrated similar hydrophobicity with water contact angles around  $80^\circ$ . When treated with BSA solution, water contact angles from these surfaces were around 60 degrees. The BSA molecule drastically increased the hydrophobicity of titanium dioxide, from  $(9 \pm 4)$  to  $(62 \pm 3)$  degrees and decreased slightly compared to that of aluminum oxide and parylene C. BSA immersion had limited influence on fused silica.

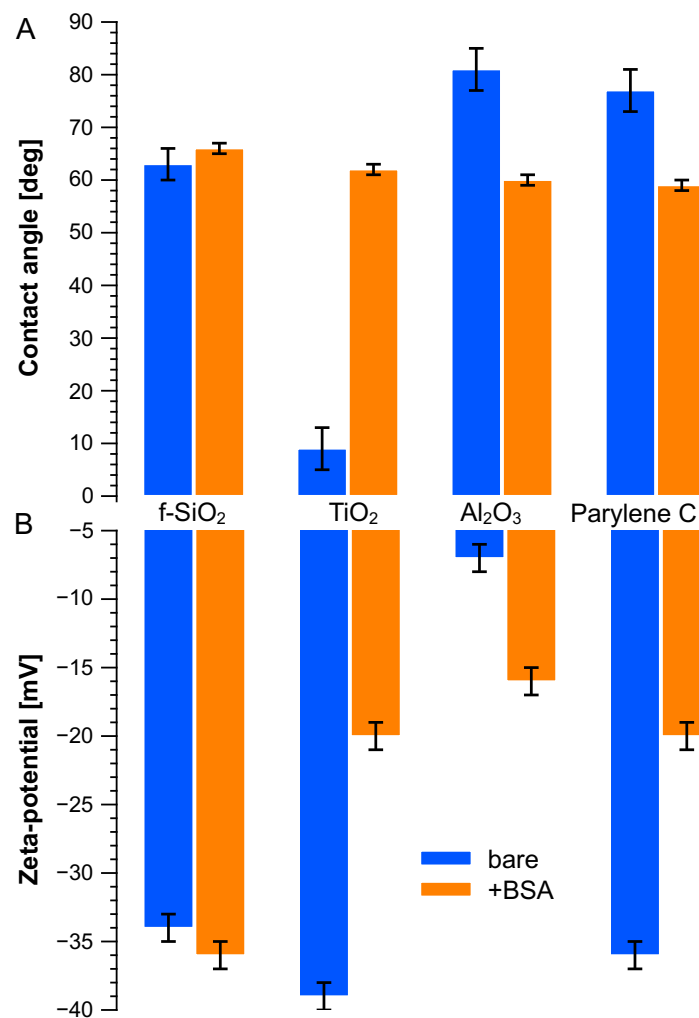


**Figure 2.** (A) Water contact angle and (B) surface zeta potential measured on bare surface (blue bars) and BSA-treated (orange bars) surfaces.

### 3.3. Zeta Potential

The zeta potentials of charged microbeads were measured as  $-110$  mV and  $+14$  mV, respectively, for carboxyl microbeads and amine microbeads under pH = 7. As for the BSA molecule, its zeta potential was measured as  $-25$  mV. The zeta potentials of the flat surface were measured using streaming potential method and are plotted in Figure 2B according to Equation (1). All surfaces show negative potential whether they were immersed in BSA or not. Titanium dioxide has the highest surface zeta potential ( $-39 \pm 1$  mV) but remains close to fused silica ( $-34 \pm 1$  mV) and parylene C ( $-36 \pm 1$  mV), while aluminum oxide has the smallest zeta potential ( $-7 \pm 1$  mV). Once treated with BSA solution, their surface charges evolved to a similar level (ca.  $-20 \pm 1$  mV) except for fused silica, which remained stable at  $-36 \pm 1$  mV.

### 3.4. Chemical Composition by XPS

The elemental composition of both bare and BSA-conditioned surfaces was determined by XPS: atomic ratios (%) are presented in Figure 3. It has to be mentioned again that the bare surfaces were analyzed after 10 mn immersion in water only. These bare surfaces exhibit a stoichiometric ratio of their constitutive elements with a few percent of residual carbon/oxygen contamination: TiO<sub>2</sub>, being a particularly reactive surface, presents the highest level of superficial contamination. No significant nitrogen was detected on these

bare surfaces. Since BSA molecule is the only source of nitrogen, the additional proportion of nitrogen after immersion in BSA solution is a good indicator to track the quantity of BSA molecule adsorbed on the surface and therefore to investigate the protein adhesion ability of these surfaces. From this criterion, it can be concluded that after 10 mn immersion in BSA solution, the most important BSA adsorption occurs on titanium dioxide, followed by fused silica, aluminum oxide, and finally very poorly on parylene C. Nevertheless, the parylene C surface was modified by a significant enrichment in oxygen that was not observed after 10 min in water alone and could thus come from adsorption of the altered BSA. By “altered BSA”, we mean adsorption of BSA that is oxygen-richer than expected. This may be due to further adsorption of hydroxyl groups that is favored by the presence of BSA since this trend is not observed when bare parylene C is immersed in water.

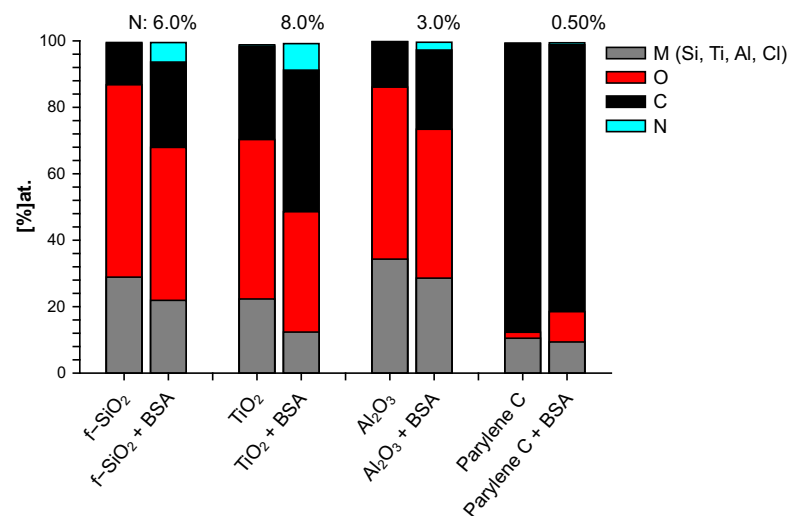


**Figure 3.** Chemical composition (% at.) of surfaces immersed 10 mn in water (bare) and 10 mn in BSA solution (+BSA).

To further investigate the adsorption of BSA and draw some hypothesis on the mechanisms, the high-resolution spectra of the various single elements were then analyzed. The objective is to identify (i) the contribution of BSA in the various spectra and (ii) the nature of the bonds that are likely to be created between BSA and the different surfaces. To facilitate the deconvolution of the spectra, an additional immersion duration in BSA solution (i.e., 24 h) was tested: this led to the increase in the protein adsorption (as shown by the evolution of nitrogen contents presented in Table 2) and in the exaltation of the trends that were initiated during the first 10 min of immersion. Results for oxides ( $\text{SiO}_2$ ,  $\text{TiO}_2$ ,  $\text{Al}_2\text{O}_3$ ) and non oxides (parylene C) are detailed as follow: a first focus on hetero atoms Ti to illustrate the oxides and Cl for Parylene—Figure 4, then on carbon and oxygen in the case of oxides (Figure 5) and parylene (Figure 6), to finish with nitrogen on both oxides ( $\text{TiO}_2$ ) and parylene (Figure 7).

**Table 2.** Evolution of the nitrogen content (at%) of the four substrates with the immersion duration in BSA solution.

Immersion Time	0	10 min	24 h
f – $\text{SiO}_2$	$0.20 \pm 0.02$	$6.0 \pm 0.2$	$10 \pm 1$
$\text{TiO}_2$	$0.45 \pm 0.05$	$8.0 \pm 0.2$	$11 \pm 1$
$\text{Al}_2\text{O}_3$	$0.10 \pm 0.02$	$3 \pm 1$	$7 \pm 1$
Parylene C	$0.20 \pm 0.05$	$0.50 \pm 0.05$	$9 \pm 1$

The spectra of Ti2p core level (see Figure 4A) for  $\text{TiO}_2$  samples are in agreement with the literature [77]: they exhibit a 5.7 eV spin-orbit split, a satellite structure around 472.3 eV,

and  $2p_{3/2}$  is located at 458.3 eV. The area ratio  $2p_{3/2} : 2p_{1/2}$  is 2:1. There is no significant evolution of this signature with the immersion in BSA solution except for the decrease in the intensity of the titanium signal. This decrease is due to the BSA adsorption on  $TiO_2$  that lowers the contribution of the  $TiO_2$  in the detected signal. As the Ti – O bond already exists on the bare surface, it is difficult to conclude on the existence of a bond between titanium and oxygen from BSA. The results (not shown here) are similar in the case of the Si2p and Al2p for respectively fused silica and alumina except for the fact that  $2p_{3/2}$  and  $2p_{1/2}$  are in the same envelope because the spin-orbit split is smaller. In the case of parylene C (see Figure 4B), Cl  $2p_{3/2}$  of the bare sample is located at 200 eV, which is consistent with chlorine in the organic compounds, with a 1.6 eV spin-orbit split and a 2:1 area ratio of  $2p_{3/2} : 2p_{1/2}$ . After 24 h immersion in BSA, Cl 2p exhibits another contribution (Cl2, with the same split and surface ratio as Cl1) at lower binding energy (197.6 eV for  $2p_{3/2}$ ), which can be attributed to BSA adsorption with a bond that is likely to be formed between chlorine and BSA amine group.

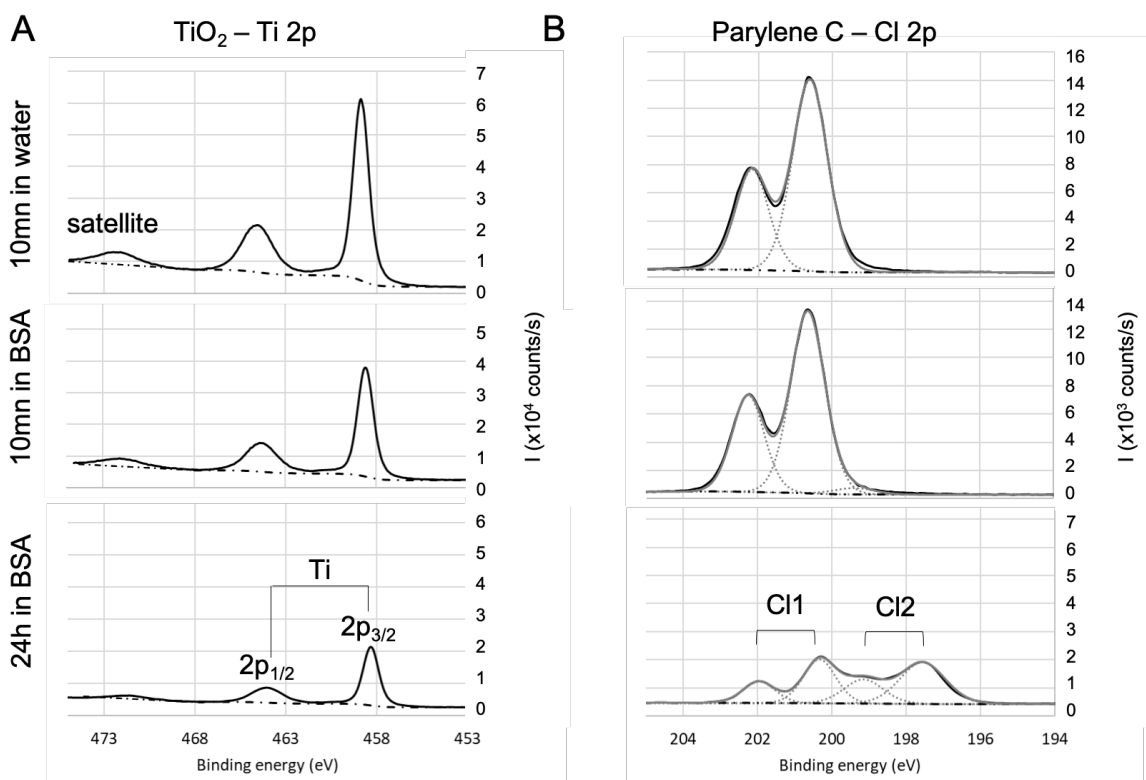


**Figure 4.** High-resolution XPS spectra of the heteroatom for (A)  $TiO_2$  and parylene C (B). Evolution with the immersion in BSA solution.

The analysis of oxygen signal was then correlated with the one of carbon. In the case of  $TiO_2$  surface (Figure 5A), the oxygen spectra exhibited three contributions of O1 (529.6 eV), O2 (531.5 eV), and O3 (532.5 eV), which can respectively be attributed to Ti – O, O = C, and O – C. The O1 atomic ratio is consistent with the stoichiometry of titania and, as the titanium signal, decreases with the immersion in BSA solution.

O2 and O3 contributions are confirmed by the analysis of carbon C1s core-level high-resolution spectra (Figure 5B). The main component of C1s is located at 285 eV and corresponds to aliphatic carbon: C – C and C – H bonds (C1). After immersion in BSA, the contributions at 286.6 eV (C2) and 288.6 eV (C3) respectively attributed to C – N, C – O, and O = C – O, O = C – N are significantly increased, confirming the presence of BSA (peptide bonds) adsorbed on the surface of titanium oxide. Moreover, the ratio  $\%N/(\%C1+\%C2)$  is close to 0.5 once the residual contamination observed on bare surface is

deduced, which is in agreement with previous work [78,79]. For fused silica and alumina, a similar conclusion can be drawn.

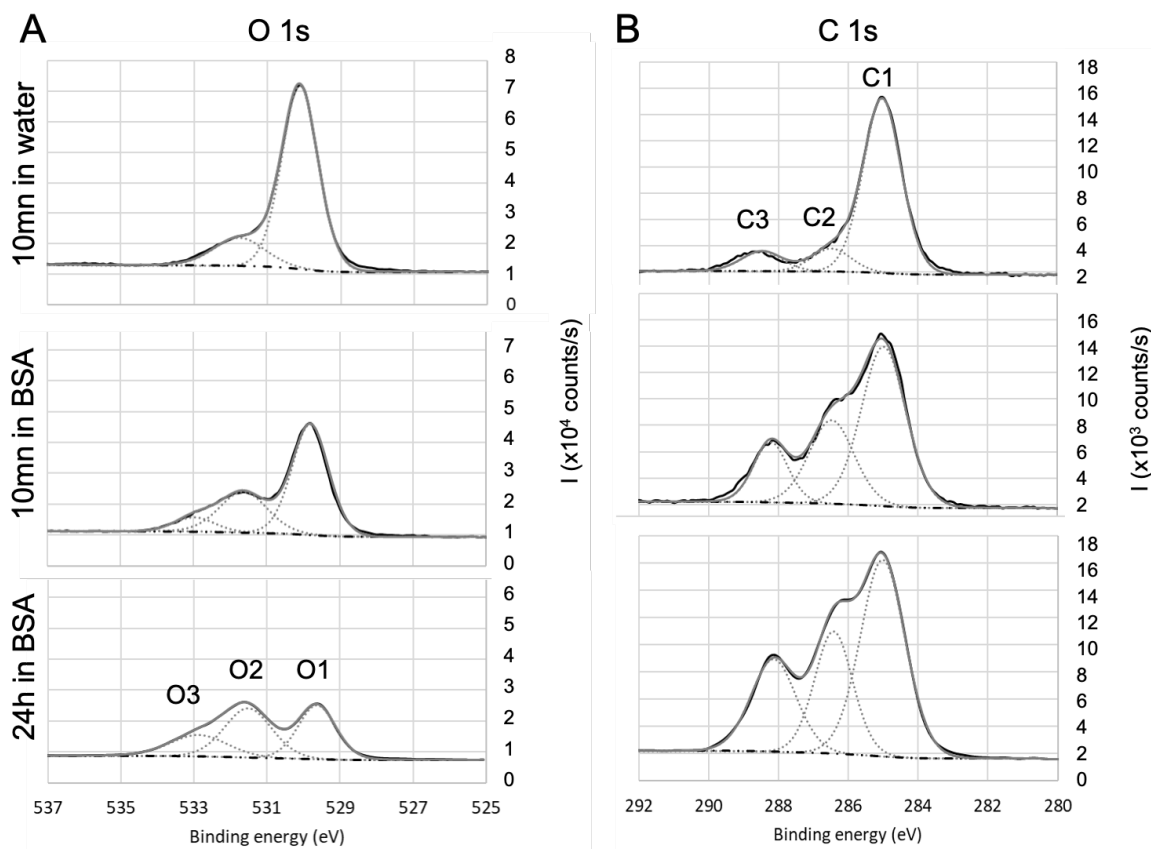


**Figure 5.** High-resolution XPS spectra of (A) oxygen and (B) carbon for  $\text{TiO}_2$ . Evolution with the immersion in BSA solution.

For parylene C, the O1s core level high-resolution spectra (Figure 6A) exhibit only O2 and O3 contributions after 24 h immersion in BSA, confirming the presence of adsorbed BSA. O2 and O3 also exist after 10 min immersion in BSA, but are less marked. On the carbon spectra (Figure 6B), C1 also includes C – C aromatic and C – Cl. The component at 291.5 eV is attributed to the satellite structure induced by  $\pi - \pi^*$  excitations on the aromatic ring [80]. After 10 mn immersion in BSA, C2 is increased compared to the bare surface and can be correlated to the increase in oxygen O2 + O3. Therefore, it can be concluded that after 10 min immersion in BSA, the surface of parylene C is enriched in oxygen: this may be due to adsorption of altered BSA due to adsorption of both BSA and hydroxyl groups as (i) the amount of adsorbed nitrogen does not match with stoichiometric BSA, (ii) C3 is too small to confirm peptide bonds and (iii) the O2+O3 contribution was lower after 10 min immersion in water alone. After 24 h immersion, the amount C2 and C3 are in agreement with O2 and O3.

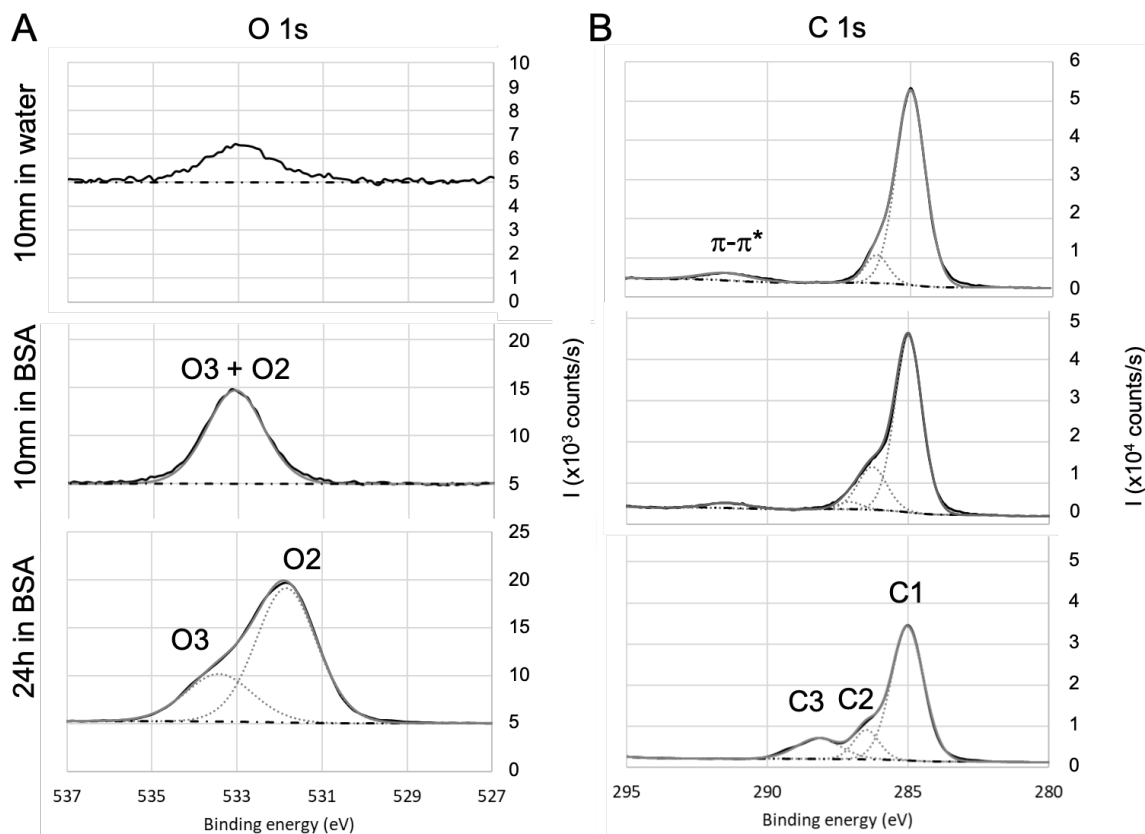


**Figure 6.** High-resolution XPS spectra of (A) oxygen and (B) carbon for parylene C. Evolution with the immersion in BSA solution.

N1s high-resolution spectra (Figure 7) after immersion in BSA exhibit N1 contribution (located at 400 eV), which is consistent with amine group (C – N bonds). N2 contribution attributed to C = N can be located in the 398–399 eV range. In the case of parylene C (Figure 7B), N3 contribution was attributed to the  $N_{BSA} - Cl_{Parylene}$  bond, which is in agreement with the Cl2 contribution observed on Figure 4B and confirmed previously by assigning this N3 contribution at 402.5 eV to  $-NH_3^+$  [69]. For titanium oxide, shown on Figure 7A, it is difficult to sharply conclude on a contribution of a  $O_{sample} - N_{BSA}$  bond because of the shape and symmetry of the N1s signal. If present, it would be around the high binding energy tail of the signal. The same observation can be made for fused silica and aluminum oxide.

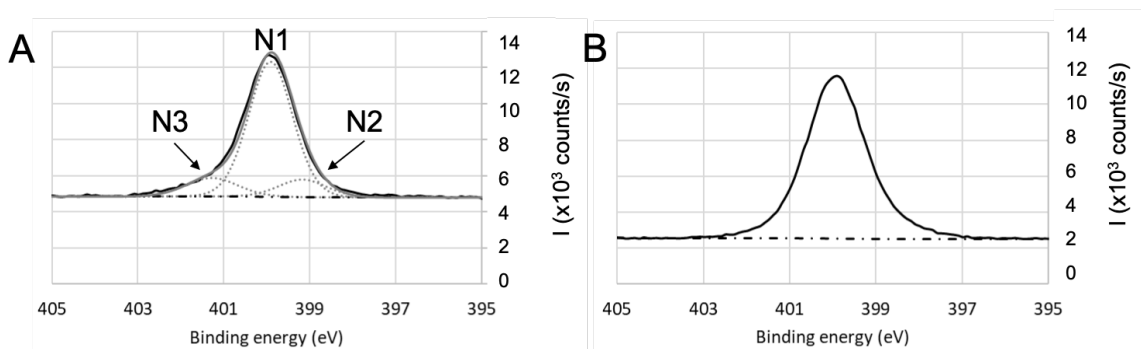


**Figure 7.** High-resolution XPS spectra of nitrogen for (A)  $TiO_2$  and (B) parylene C after a 24 h-immersion in BSA solution

The composition of the adsorbed layer was finally investigated in terms of N/O, N/(C1 + C2) and N/C ratios and compared to BSA stoichiometric composition [81]. The con-

tribution of the bare substrate was subtracted from the global quantitative analysis, considering that the composition of the substrate was stoichiometric: the evaluation of this contribution was deduced from the amount of the heteroatom. The results are presented in Figure 8. Globally, whatever the immersion duration, all the adsorbed layers exhibit an excess in the carbon amount. After 10 min immersion, the N/O ratio is higher than the reference on silica fume and lower on alumina and titanium dioxide. Considering that the N/(C1+C2) ratio matches with the reference for f-SiO<sub>2</sub> and TiO<sub>2</sub>, this means that the adsorbed layer is oxygen-deficient for f-SiO<sub>2</sub> and presents an excess in oxygen on TiO<sub>2</sub>. On alumina, the superficial layer is nitrogen-deficient. After 24 h immersion, except for the excess on contamination carbon, the adsorbed superficial layer is rather close to BSA composition on fused silica and alumina whereas it remains too rich in oxygen on parylene C and titanium dioxide.

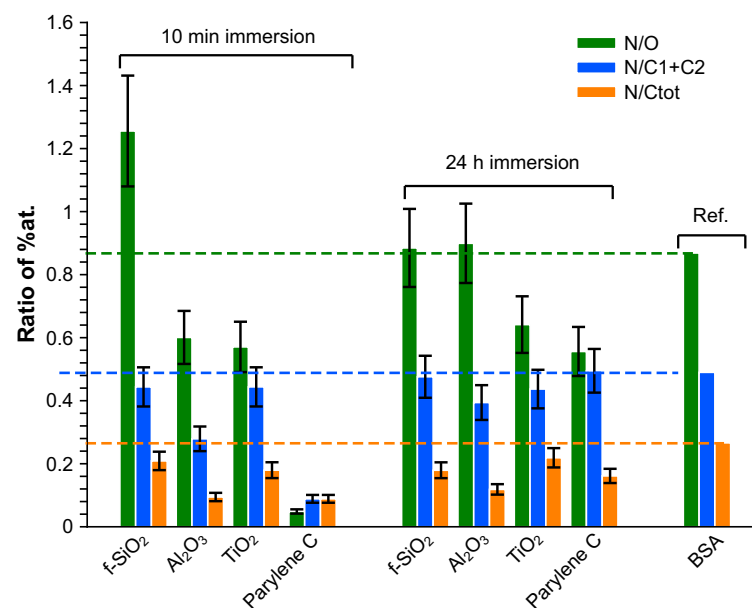


**Figure 8.** Elemental composition of the adsorbed layer.

### 3.5. Microbeads Adhesion to Surfaces

Shear-induced detachment of the two types of beads was monitored by video microscopy. The wall shear stress required to remove half the initial population  $\tau_w^{50}$  is reported in Table 3 according to the surfaces tested and the type of microbead. Therefore, the lower  $\tau_w^{50}$  value, the better anti-adhesion performance. When this value is not reached, meaning that more than 50% of microbeads were still on the surface in the end of experiment, the surface exhibits adhesive properties. When no detachment occurs, this value can reach 80 Pa (the maximum value obtained in this setup).

**Table 3.**  $\tau_w^{50}$  value of bare and BSA-treated (+BSA) surfaces measured in shear stress flow chamber using positively charged (NH<sub>2</sub>(+)) and negatively charged (COOH(-)) polystyrene microbeads. In case the detached number of beads did not reach down the half population,  $\tau_w^{50}$  displays n/a.

$\tau_w^{50}$ (Pa)	NH <sub>2</sub> (+)		COOH(-)	
	bare	+BSA	bare	+BSA
f-SiO <sub>2</sub>	1.1 ± 0.3	23 ± 7	5 ± 3	n/a
TiO <sub>2</sub>	17 ± 4	9 ± 4	n/a	n/a
Al <sub>2</sub> O <sub>3</sub>	2 ± 1	1.1 ± 0.3	24 ± 9	9 ± 3
Parylene C	5 ± 2	3 ± 2	22 ± 6	n/a

For both microbeads, with positive or negative charge, titanium dioxide showed significant adhesion to surfaces, higher than the three other materials, and fused silica exhibited the smallest  $\tau_w^{50}$  value. Besides, negatively charged microbeads adhere steadier on the surface than positively charged microbeads, in general. When treated with 1 g/L BSA solution, the performance of these materials varies: the adhesion of both microbeads remarkably increased on fused silica and decreased on aluminum oxide. However, the situation tends to be different on titanium dioxide and parylene C. On titanium dioxide, adsorbed BSA reduced the adhesion of positively charged microbeads and did not affect that of negatively charged microbeads. On parylene C, adsorbed BSA slightly reduced the adhesion of positively charged microbeads but enhanced that of negatively charged microbeads.

#### 4. Discussion

This study delves into the investigation of how Bovine Serum Albumin (BSA), employed as a model protein for conditioning immersed surfaces, adsorbs under low ionic strength [79]. The research is conducted within the framework of immersed monitoring optical sensors, with X-ray Photoelectron Spectroscopy (XPS) serving as the primary analytical tool for scrutinizing the adsorption of BSA onto various materials [79], aiming to mitigate biofouling concerns. To fortify our findings, we employed microbeads functionalized with carboxyl or amine groups within a shear-flow chamber [45,69,75]. This approach allows for a comprehensive evaluation of adhesion properties. Furthermore, Principal Component Analysis (PCA) was implemented and presented in this section to elucidate potential correlations between substrate and microbead surface properties.

##### 4.1. Analysis of BSA Adsorption

The adsorption of BSA was investigated by plotting the data presented in Table 4. Not-reached values of  $\tau_p^{50}$  were estimated and ranked from the detachment profiles in order to allow the PCA calculation.

**Table 4.** Dataset used for the principal components PCA1 and PCA2.  $\tau_w^{50-}$  and  $\tau_w^{50+}$  represent the  $\tau_w^{50}$  of carboxyl and manie microbeads, respectively.

Surface	$R_q$ (nm)	$\theta_w$ (°)	$\zeta$ (mV)	$\tau_w^{50+}$ (Pa)	$\tau_w^{50-}$ (Pa)	%N (%at.)
f – SiO <sub>2</sub>	0.7 ± 0.1	63 ± 3	34 ± 1	1.1 ± 0.3	5 ± 3	6.0 ± 0.2
TiO <sub>2</sub>	15 ± 2	9 ± 4	−39 ± 1	17 ± 4	80 ± 3	8.0 ± 0.2
Al <sub>2</sub> O <sub>3</sub>	1.5 ± 0.2	81 ± 4	−7 ± 1	2 ± 1	24 ± 9	3 ± 1
Parylene C	2.0 ± 0.2	77 ± 3	−36 ± 1	5 ± 2	22 ± 6	0.50 ± 0.05

For this first PCA analysis, all the variables are active (as they participate to the PC building). The data are correctly represented (about 90% of the information, see Figure 9A) in a 2D coordinate system where the first principal component (PC1) can be assimilated to roughness, water contact angle, and adhesion of functionalized beads whereas PC2 is correlated to zeta potential (Figure 9B). The nature of PC1 indicates that both roughness and hydrophilicity (i.e., small water contact angle) strongly favor the adhesion of microbeads (whether positively or negatively charged), whereas the  $\zeta$  potential of substrates appears uncorrelated.

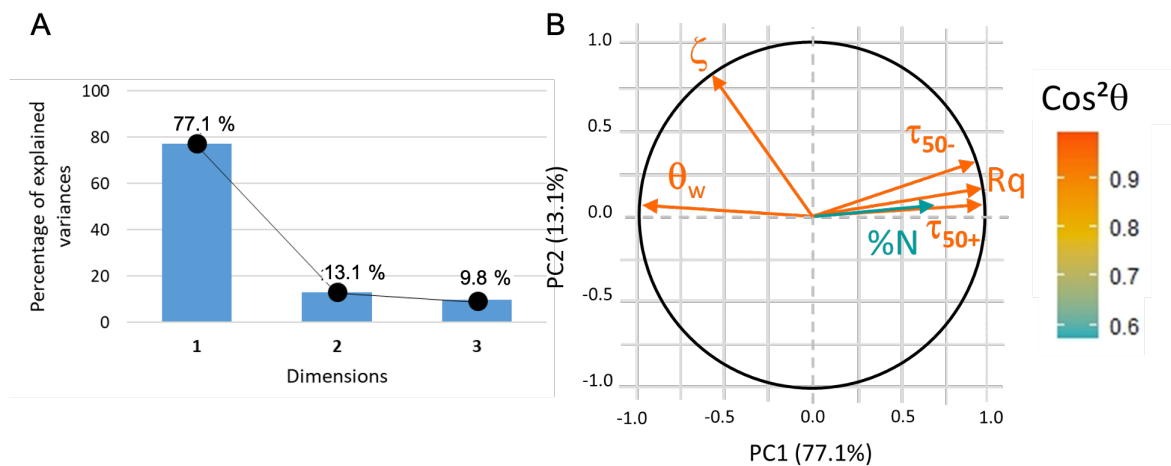


**Figure 9.** (A) PCA1 variance plot that shows that 90% of the information is described by PC1 and PC2. (B) Loading plot where  $\text{cos}^2\theta$  indicates that only protein adsorption data is not correctly represented.

In the context of this 2D system, the adsorption of protein is partially elucidated and appears to closely align with the first principal component (PC1). Subsequently, an additional principal component analysis was conducted, omitting consideration of the zeta potential values due to their lack of correlation with the remaining dataset. This exclusion finds validation in the experimental observation that BSA adsorption takes place in immersion media characterized by a slightly higher ionic strength compared to that employed in zeta potential measurements for both microbeads and surfaces. It can be hypothesized that, during the BSA adsorption phase, the surface zeta potential of the immersed substrates is likely obscured by the presence of other charges in the solution and may not exert a significant influence. This observation is further supported by the empirical finding that negatively charged microbeads exhibited stronger adhesion to the substrates compared to positively charged counterparts, notwithstanding the negative zeta potential exhibited by all substrates.

In this new plotting system, the adsorption of BSA is much better represented (Figure 10). It is positively linked to roughness and hydrophilicity, but also depends on another factor, PC2, which remains to be identified. The score plot positions  $\text{TiO}_2$  and  $\text{Al}_2\text{O}_3$  surfaces along PC1 while parylene C,  $\text{Al}_2\text{O}_3$  and f-SiO<sub>2</sub> are along PC2 (see Figure 11). In other words, considering protein adsorption, alumina and titanium dioxide mainly differ in roughness and hydrophilicity whereas parylene C,  $\text{Al}_2\text{O}_3$  and f-SiO<sub>2</sub> are essentially discriminated by PC2.

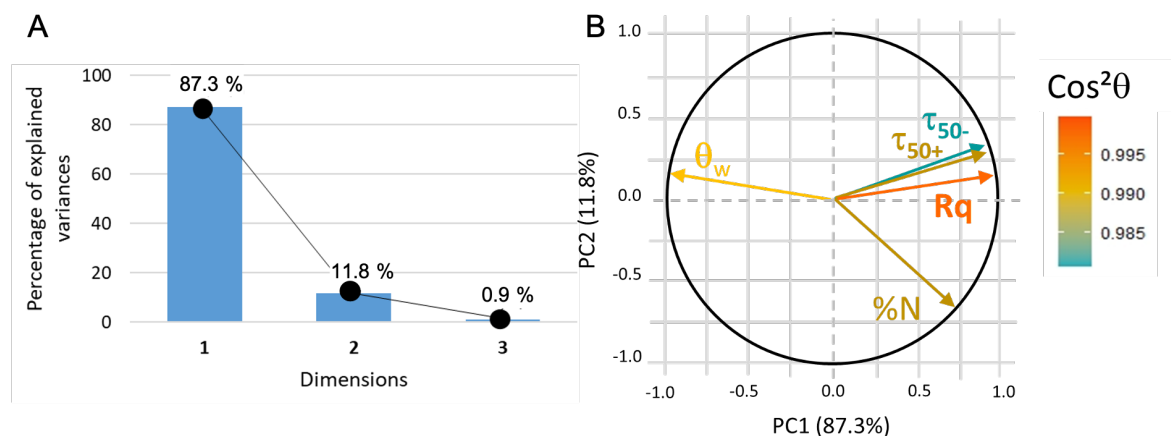


**Figure 10.** (A) PCA2 variance plot that shows that 98% of the information is described by PC1 and PC2. (B) Loading plot where  $\text{cos}^2\theta$  indicates that all the data are correctly represented.

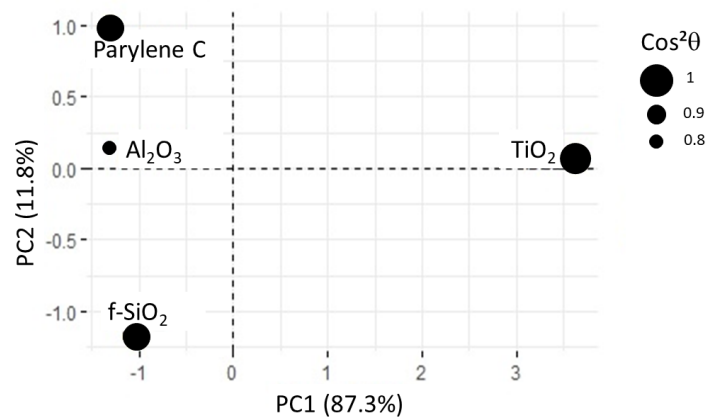


**Figure 11.** Score plot for PCA2. All the substrates are correctly represented, as shown by  $\cos^2\theta$  values. For alumina surface,  $\cos^2\theta$  is close to 0.8.

This first analysis on protein adsorption is in agreement with results from literature [82,83]. Surface roughness, in a nanometric range, as well as hydrophilicity, strongly influence protein adsorption, while zeta potential does not seem to be significant. An additional component is missing to further describe the interaction between surface and protein. The component that discriminates parylene C, alumina, titanium oxide, and fused silica could be correlated to the nature of the bonds involved in each material. The bonds drive the charge distribution at the surface and thus the reactivity and the adsorption sites. By considering the Pauling electronegativity of each element, fused silica is  $\sim 60\%$  covalent whereas aluminum oxide and titanium are rather  $\sim 60\%$  ionic: the electrons delocalization in ionic compounds favors reactivity and adsorption. Parylene C is mostly covalent, but the presence of polar chlorine atom induces a dipole: chlorine appears to be a preferential adsorption site, which was confirmed by XPS analysis. The lower adsorption rate on parylene C in the earlier adsorption steps is due to reduced number of adsorption sites in comparison with ionic-covalent compounds. The importance of the surface charge distribution on protein adhesion was pointed out by Beragoui et al. [84]. They studied BSA adsorption on differently functionalized polystyrene surfaces, demonstrating the important contribution of hydrogen bonds in the adsorption, compared to hydrophobic and electrostatic interactions. Ab initio calculation coupled to adsorption isotherm experiments would be useful to further investigate the local charge distribution on each surface and the resulting adsorption scenario and kinetics.

#### 4.2. Influence of the Conditioning Film on the Adhesion of Functionalized Hydrophobic Polystyrene Microbeads

To analyze the influence of BSA adsorption on the adhesion of the functionalized microbeads, PCA-3 was run in two steps, considering the data presented in Table 5. Once the appropriate coordinate system was found to describe the surfaces before immersion in BSA, the surfaces after immersion were plotted in this 2D system. In statistical terms, PCA-3 was run considering surface description before immersion in BSA as “active individuals” and surface description after immersion as “supplementary individuals”.

**Table 5.** The dataset used for PCA3. The first step consists of determining the PCs, and the second step determines the influence of the BSA surface conditioning.

PCA3	Surface	$\theta_w$ (°)	$\zeta$ (mV)	$\tau_w^{50+}$ (Pa)	$\tau_w^{50-}$ (Pa)
1st step	f – SiO <sub>2</sub>	63 ± 3	−34 ± 1	1.1 ± 0.3	5 ± 3
	TiO <sub>2</sub>	9 ± 4	−39 ± 1	17 ± 4	80 ± 3
	Al <sub>2</sub> O <sub>3</sub>	81 ± 4	−7 ± 1	2 ± 1	24 ± 9
	Parylene C	77 ± 3	−36 ± 1	5 ± 2	22 ± 6
2nd step + BSA	f – SiO <sub>2</sub>	66 ± 4	−36 ± 1	23 ± 7	80 ± 3
	TiO <sub>2</sub>	62 ± 4	−20 ± 1	9 ± 4	65 ± 3
	Al <sub>2</sub> O <sub>3</sub>	60 ± 4	−16 ± 1	1.1 ± 0.3	9 ± 3
	Parylene C	59 ± 6	−20 ± 1	3 ± 2	50 ± 3

The data plot in the 2D coordinate system (with hydrophilicity as PC1 and PC2 partially correlated to surface zeta potential, see Figure 12) indicates that, without conditioning film, the adhesion of microbeads, whether positively or negatively charged, is mainly driven by hydrophilicity. Nevertheless, the adhesion is systematically stronger in the case of carboxyl-microbeads.

After immersion of the surfaces in BSA, the evolution of the adhesion of microbeads depends on the surface, as illustrated by the score plot (Figure 13). All the sample are correctly represented by PC1 and PC2, except for f – SiO<sub>2</sub> in BSA, which presents 0.6 as  $\cos^2\theta$  and a significant coordinate on PC3. Anyway, the comparison of f – SiO<sub>2</sub> before and after immersion in BSA remains reliable as the change in the coordinate along PC1 and PC2 is quite significant. On Al<sub>2</sub>O<sub>3</sub> and parylene C, the adhesion is poorly affected, whereas it is drastically increased on f – SiO<sub>2</sub> and significantly decreased on TiO<sub>2</sub>. This behavior is observed for both functional groups, but it is emphasized in the case of carboxyl-microbeads. This can be explained by the ionic-covalent nature of bonds: on covalent fused-silica, the protein conditioning film creates polar adsorption sites (–COO– and –NH<sub>3</sub><sup>+</sup>). On aluminum oxide, titanium dioxide and parylene C, BSA is likely to create polar sites on a surface that already had some. Therefore, no change on microbeads adhesion is observed on aluminum oxide and parylene C. In the case of titanium dioxide, adhesion property is reduced because of the modification of hydrophilicity, which is in line with protein adsorption. The immersion of the surfaces in BSA reduces the dispersion of the samples regarding PC2, which could be the correlation between zeta potential and the ionic-covalent nature of bonds. Finally, as the BSA-samples do not have all the same coordinates, we can assume that the immersed surface are different: in other words, they are either not fully covered by BSA or BSA adhered in different conformations, as suggested in previous works [85]. Devlopoulos et al. [86] also observed that BSA adsorbed differently regarding the nature of the substrate: dense layers are formed on parylene C whereas thicker and more diffuse layers develop on silicon oxide. Further analysis with FTIR and Raman microscopy as well as AFM adhesion force mapping need to be performed to characterize the coverage homogeneity as well as the BSA conformation [87].

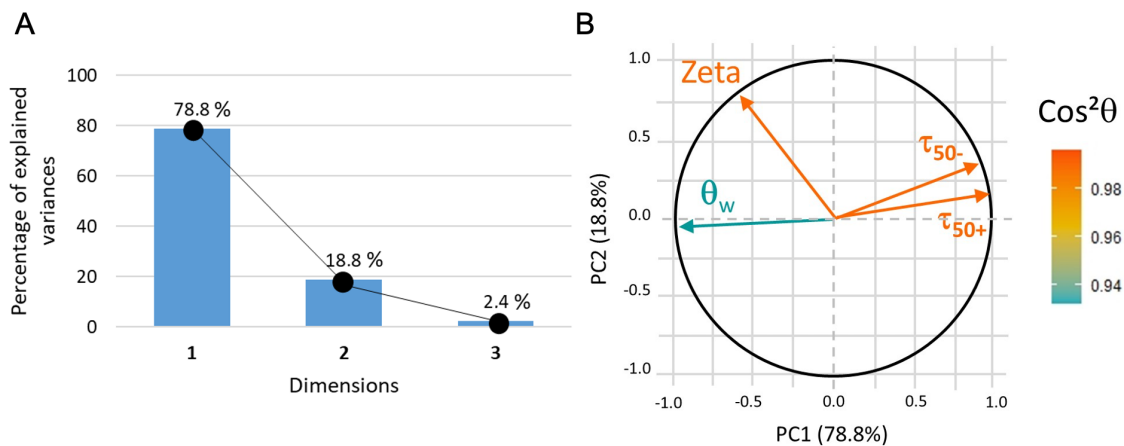


**Figure 12.** (A) PCA3 variance plot that shows that 97% of the information is described by PC1 and PC2. (B) Loading plot where  $\text{cos}^2\theta$  indicates that all the data correctly represented.

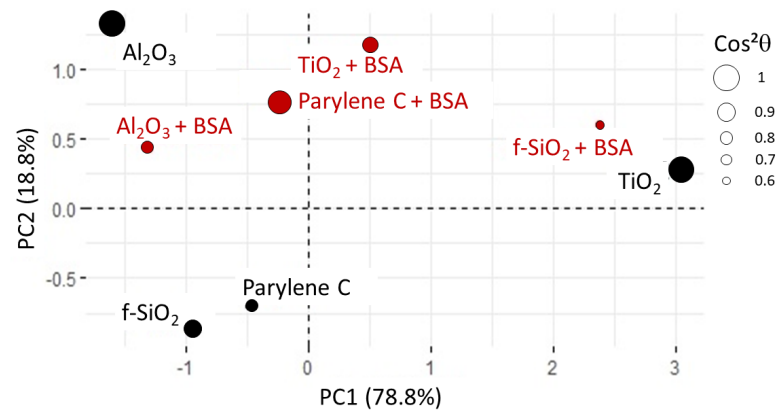


**Figure 13.** Score plot for PCA3. The  $\text{Cos}^2\theta$  values shows that the representation of fused silica in BSA is the least reliable (0.6 for f – SiO<sub>2</sub>). All the other samples are correctly represented with  $\text{cos}^2\theta$  ranging from 0.76 to 1.

#### 4.3. Towards the Adsorption of Microorganisms

As alluded to above, the primary objective of this investigation is to elucidate the adsorption behavior of Bovine Serum Albumin (BSA), employed as a model protein, in order to assess its interaction with modified surfaces, with the ultimate aim of proffering potential strategies for anti-fouling surface development. The empirical foundation of this inquiry rests upon an in-depth examination of microbead adhesion properties under controlled flow conditions, subsequently correlated with pertinent surface properties. In light of these achievements, the subsequent phase of our research endeavors will entail subjecting these surfaces to microbial organisms—an aspect not within the immediate purview of this study, yet one that merits discussion in the ensuing section and represents a prospective avenue for further inquiry.

The conclusion on the influence of hydrophilicity on microbeads adhesion is consistent with results on hydrophobic bacteria from literature. Some earlier studies pointed out that substrate surface hydrophobicity is an important factor for bacterial adhesion, where a superhydrophobic surface significantly reduced the adhesion of some hydrophobic bacteria such as *Escherichia coli*, *Staphylococcus aureus*, and *Pseudomonas aeruginosa* [88–90]. By using hydrophobic bacteria *E. coli*, Friedlander et al. [91] observed an increase of bacterial

adhesion as polydimethylsiloxane (PDMS) surface status changing from non-wetting to wetting. Lu et al. [92] also demonstrated a decrease of *E.coli* coverage rate due to the surface becoming more hydrophobic. On the contrary, Thewes et al. [93] did a single-cell force spectroscopy study with hydrophilic bacteria *Staphylococcus carnosus*, indicating that unspecific bacterial adhesion is governed by hydrophobic interaction and decreases as the surface became more hydrophilic. This hydrophilic repulsion, which was subjected by hydration pressure [73] between microorganisms and surfaces, displaying hydrophilic properties, was also pointed out previously, with yeast cells experiencing a decrease of such repulsion with an increase in ionic strength [94].

In addition to hydrophobicity concerns, in aqueous environments, the prevailing forces are typically Lifshitz–van der Waals (LW) and electrostatic (EL) forces, as outlined in [95] following the DLVO theory, which stands for Derjaguin–Landau–Verwey–Overbeek. Given that microorganisms and most synthetic and natural surfaces carry a negative charge at typical pH levels, electrostatic interactions are generally repulsive. At low ionic strength (1 mM), the long-range DLVO-type electrostatic repulsion takes precedence over van der Waals attraction [94]. However, under high ionic strength conditions, van der Waals attraction becomes dominant [57,95–97]. Nonetheless, the DLVO theory has only seen limited success in elucidating microbial adhesion phenomena on diverse surfaces. This is due to its failure to account for non-DLVO interactions, such as hydrophobicity and hydrophilicity, as expounded by the extended DLVO theory [73,98–102].

However, consideration must be given that the composition of the microbial cell surface deviates markedly from that of a hydrophobic colloid. This surface is predominantly constituted of biopolymers, exhibiting variable degrees of solvation. Consequently, the intermolecular interactions occurring at this interface assume pivotal importance. These interactions may encompass the establishment of covalent bonds between specific segments of the macromolecular species and the substrate surface. Furthermore, microbial cells exhibit an active capacity to release macromolecules into the surrounding milieu. This dynamic process expeditiously conditions the substrate surface through adsorption as modeled in this project by BSA, thereby establishing a conducive environment for cellular adhesion [103]. Empirical validation of this phenomenon has been provided, specifically in the context of *Azospirillum brasilense* [104]. The interplay between the conditioned surface and microbial cells is further nuanced, potentially involving bridging interactions between segments of the macromolecular entities. Such interactions are notably potentiated by increased ionic strength and the presence of divalent cations. Moreover, specific interactions have been observed in instances of mammalian cell–substrate interactions, particularly when the substrate has been conditioned by protein adsorption [105].

Concerning the influence of surface nano-roughness on the adhesion of microorganisms, the literature remains conflicting. Some studies suggested that cell adhesion was favored on a nano-rough surface [106] whereas others showed a better adhesion in the case of a nano-smooth surface [107,108]. The impact of surface roughness has to be considered globally:  $R_a$  or  $R_q$  are not sufficient to correctly describe the topography: shapes, texturing, and aspect ratio should also be taken into account [109,110]. Vellido-Rodríguez et al. [111] reported that the adhesion of both *Staphylococcus epidermidis* and *Staphylococcus aureus* was significantly reduced by engineered surface patterns with nanometer vertical dimensions (i.e., smaller than cell dimension), suggesting that the singular points designed on the surface (i.e., square corners, convex walls) drove the initial cell location and could further interfere with cell–cell communication and thus biofilm growth.

Finally, the impact of the conditioning film on cell adhesion is reported to be strongly dependent on the nature of the substrate that drives the formation of this conditioning layer, as well as the ionic strength of the immersion media. In Ref. [86], the authors showed that parylene C and silicon oxide, after immersion in the same protein serum, exhibit drastically different conditioning film, resulting in much higher cell adhesion on silicon oxide. This trend was also observed by Hwang et al. [62] for *Burkholderia cepacia* on BSA-

coated silica slides but only at low ionic strength (in 1 mM KCl). At higher ionic strength, BSA conditioning film significantly hindered bacterial adhesion.

## 5. Conclusions

In the realm of environmental observatories and the pressing need to develop innovative approaches for reducing biofouling on autonomous optical sensors deployed in continental waters, this study focuses on exploring the relationship between the physico-chemical characteristics of coated or nanostructured surfaces and their susceptibility to the adhesion of precisely calibrated solid particles. Additionally, the inquiry encompasses situations where model conditioning proteins are present. The primary objective was to suggest anti-fouling surfaces that deter protein adsorption (BSA) and establish a connection to the subsequent initial adhesion of particles. Two simplistic functions were selected (carboxyl and amine), which are usually encountered on microorganisms.

In this context, four distinct surfaces (fused silica, titanium dioxide, aluminum oxide, and parylene C) were evaluated both before and after being immersed in BSA solution. The assessment involved parameters such as roughness, surface charge, water contact angle, surface composition of the substrates, and interaction with functionalized microbeads, which served as models for simplified microorganisms.

The findings indicate that protein adsorption was primarily influenced by surface roughness at a submicrometric scale, hydrophilicity, and likely connected to the electron distribution on the surface, hence, the type of bonds present on the material surface. Among the surfaces, titanium dioxide exhibited the highest adsorption properties, while parylene C showed a lower kinetic rate.

In terms of protein adsorption mechanisms, clear evidence of bonds between amine groups and chlorine is observed on parylene C. However, on the oxide, there is no conclusive indication of the formation of Moxide-OBSA or Ooxide-NBSA bonds, or both. Both scenarios are plausible, and further investigation through *ab initio* and molecular dynamic calculations is needed.

After a 24-h immersion in BSA solution, alumina and silica developed a conditioning film with a composition closely resembling that of BSA, whereas an excess of oxygen was noted on titanium dioxide and parylene C.

This conditioning film had varying effects on surface interactions with microbeads, influencing hydrophilicity as well as the local distribution of charges. Fused silica experienced a substantial increase in microbead adhesion, while parylene C showed a milder effect, and titanium dioxide displayed reduced adhesion. Alumina distinguished itself for its stability, as the growth of the conditioning film has a limited impact on its adhesion properties, which remain relatively low.

To comprehensively assess the influence of the conditioning film on microbial adhesion, further studies need to be conducted, incorporating experiments involving relevant microorganisms.

**Author Contributions:** Z.N. performed the shear stress flow experiments, and the physico-chemical characterization of the microbeads. C.T. developed the surfaces and performed the XPS and AFM analysis. P.F. developed the PCA analysis and its interpretation. D.C. designed and supervised the PhD work of Z.N. M.C. supervised the PhD work of Z.N., designed and interpreted the shear stress experiments and microbeads characterization, and managed the overall writing process of this manuscript. Conceptualization, C.T. and M.C.; methodology, Z.N., D.C., C.T., and M.C.; software, Z.N., C.T., M.C., and P.F.; validation, C.T., M.C., and P.F.; formal analysis, C.T., M.C., and P.F.; resources, C.T. and M.C.; data curation, Z.N., C.T., P.F., and M.C.; writing—original draft preparation, Z.N., C.T., and M.C.; writing—review and editing, M.C.; supervision, C.T., M.C., and D.C.; project administration, C.T., M.C., and D.C.; funding acquisition, C.T. and M.C. All authors have read and agreed to the published version of the manuscript.

**Funding:** This research was funded by INPT-INSA (local funding), ANDRA, and Chinese Scholarship Council (Z.N. PhD scholarship).

**Institutional Review Board Statement:** Not applicable.

**Informed Consent Statement:** Not applicable.

**Data Availability Statement:** All data are available upon request.

**Acknowledgments:** We thank Jerome Esvan for performing the XPS measurements as well as Justyna Junca for her preliminary investigations on alumina surfaces and our training students Jane Jandel and Yanzhu Tao for their contribution to the shear stress flow chamber experiments. We are grateful to Philippe Schmitz for the discussions on shear-stress flow results analysis and conceptualization of the setup.

**Conflicts of Interest:** The authors declare no conflict of interest. The funders had no role in the design of the study; in the collection, analyses, or interpretation of data; in the writing of the manuscript; or in the decision to publish the results.

### Abbreviations

The following abbreviations are used in this manuscript:

AFM	Atomic Force Microscopy
BSA	Bovine Serum Albumin
TiO <sub>2</sub>	Titanium dioxide
f – SiO <sub>2</sub>	Silica fuse
Al <sub>2</sub> O <sub>3</sub>	Alumina
XPS	X-ray Photoelectron Spectroscopy

### References

1. Delgado, A.; Briciu-Burghina, C.; Regan, F. Antifouling Strategies for Sensors Used in Water Monitoring: Review and Future Perspectives. *Sensors* **2021**, *21*, 389. [[CrossRef](#)] [[PubMed](#)]
2. Delauney, L.; Compère, C.; Lehaitre, M. Biofouling protection for marine environmental sensors. *Ocean. Sci.* **2010**, *6*, 503–511. [[CrossRef](#)]
3. Tendero, C.; Lazar, A.M.; Samélor, D.; Debieu, O.; Constantoudis, V.; Papavieros, G.; Villeneuve, A.; Vahlas, C. Nanocomposite thin film of Ag nanoparticles embedded in amorphous Al<sub>2</sub>O<sub>3</sub> on optical sensors windows: Synthesis, characterization and targeted application towards transparency and anti-biofouling. *Surf. Coatings Technol.* **2017**, *328*, 371–377. [[CrossRef](#)]
4. Fletcher, M. Bacterial biofilms and biofouling. *Curr. Opin. Biotechnol.* **1994**, *5*, 302–306. [[CrossRef](#)]
5. Costerton, J.W.; Stewart, P.S.; Greenberg, E.P. Bacterial Biofilms: A Common Cause of Persistent Infections. *Science* **1999**, *284*, 1318–1322. [[CrossRef](#)] [[PubMed](#)]
6. Costerton, J.W.; Lewandowski, Z.; Caldwell, D.E.; Korber, D.R.; Lappin-Scott, a.H.M. Microbial Biofilms. *Annu. Rev. Microbiol.* **1995**, *49*, 711–745. [[CrossRef](#)] [[PubMed](#)]
7. Qiu, H.; Feng, K.; Gapeeva, A.; Meurisch, K.; Kaps, S.; Li, X.; Yu, L.; Mishra, Y.K.; Adelung, R.; Baum, M. Functional polymer materials for modern marine biofouling control. *Prog. Polym. Sci.* **2022**, *127*, 101516. [[CrossRef](#)]
8. Srey, S.; Jahid, I.K.; Ha, S.D. Biofilm formation in food industries: A food safety concern. *Food Control.* **2013**, *31*, 572–585. [[CrossRef](#)]
9. Costerton, J.W.; Montanaro, L.; Arciola, C.R. Biofilm in implant infections: Its production and regulation. *Int. J. Artif. Organs* **2005**, *28*, 1062–1068. [[CrossRef](#)]
10. Donlan, R.M.; Costerton, J.W. Biofilms: Survival mechanisms of clinically relevant microorganisms. *Clin. Microbiol. Rev.* **2002**, *15*, 167–192. [[CrossRef](#)]
11. Navarro-Villoslada, F.; Orellana, G.; Moreno-Bondi, M.C.; Vick, T.; Driver, M.; Hildebrand, G.; Liefelth, K. Fiber-Optic Luminescent Sensors with Composite Oxygen-Sensitive Layers and Anti-Biofouling Coatings. *Anal. Chem.* **2001**, *73*, 5150–5156. [[CrossRef](#)]
12. Whelan, A.; Regan, F. Antifouling strategies for marine and riverine sensors. *J. Environ. Monit.* **2006**, *8*, 880. [[CrossRef](#)] [[PubMed](#)]
13. Champ, M.A. A review of organotin regulatory strategies, pending actions, related costs and benefits. *Sci. Total. Environ.* **2000**, *258*, 21–71. [[CrossRef](#)] [[PubMed](#)]
14. Gipperth, L. The legal design of the international and European Union ban on tributyltin antifouling paint: Direct and indirect effects. *J. Environ. Manag.* **2009**, *90* (Suppl. S1), S86–S95. [[CrossRef](#)] [[PubMed](#)]
15. Uc-Peraza, R.G.; Castro, B.; Fillmann, G. An absurd scenario in 2021: Banned TBT-based antifouling products still available on the market. *Sci. Total. Environ.* **2022**, *805*, 150377. [[CrossRef](#)] [[PubMed](#)]
16. Li, J.H.; Shao, X.S.; Zhou, Q.; Li, M.Z.; Zhang, Q.Q. The double effects of silver nanoparticles on the PVDF membrane: Surface hydrophilicity and antifouling performance. *Appl. Surf. Sci.* **2013**, *265*, 663–670. [[CrossRef](#)]

17. Saulou, C.; Despax, B.; Raynaud, P.; Zanna, S.; Marcus, P.; Mercier-Bonin, M. Plasma deposition of organosilicon polymer thin films with embedded nanosilver for prevention of microbial adhesion. *Appl. Surf. Sci.* **2009**, *256*, S35–S39. [[CrossRef](#)]
18. Banerjee, S.; Dionysiou, D.D.; Pillai, S.C. Self-cleaning applications of TiO<sub>2</sub> by photo-induced hydrophilicity and photocatalysis. *Appl. Catal. B Environ.* **2015**, *176–177*, 396–428. [[CrossRef](#)]
19. Barthomeuf, M.; Castel, X.; Le Gendre, L.; Louis, J.; Denis, M.; Pissavin, C. Effect of Titanium Dioxide Film Thickness on Photocatalytic and Bactericidal Activities Against *Listeria monocytogenes*. *Photochem. Photobiol.* **2019**, *95*, 1035–1044. [[CrossRef](#)]
20. Choi, H.; Sofranko, A.C.; Dionysiou, D.D. Nanocrystalline TiO<sub>2</sub> Photocatalytic Membranes with a Hierarchical Mesoporous Multilayer Structure: Synthesis, Characterization, and Multifunction. *Adv. Funct. Mater.* **2006**, *16*, 1067–1074. [[CrossRef](#)]
21. Noguchi, T.; Fujishima, A.; Sawunyama, P.; Hashimoto, K. Photocatalytic Degradation of Gaseous Formaldehyde Using TiO<sub>2</sub> Film. *Environ. Sci. Technol.* **1998**, *32*, 3831–3833. [[CrossRef](#)]
22. Ohko, Y.; Utsumi, Y.; Niwa, C.; Tsumata, T.; Kobayakawa, K.; Satoh, Y.; Kubota, Y.; Fujishima, A. Self-sterilizing and self-cleaning of silicone catheters coated with TiO<sub>2</sub> photocatalyst thin films: A preclinical work. *J. Biomed. Mater. Res.* **2001**, *58*, 97–101. [[CrossRef](#)] [[PubMed](#)]
23. Paz, Y.; Heller, A. Photo-oxidatively self-cleaning transparent titanium dioxide films on soda lime glass: The deleterious effect of sodium contamination and its prevention. *J. Mater. Res.* **1997**, *12*, 2759–2766. [[CrossRef](#)]
24. Hölken, I.; Hoppe, M.; Mishra, Y.K.; Gorb, S.N.; Adelung, R.; Baum, M.J. Complex shaped ZnO nano- and microstructure based polymer composites: Mechanically stable and environmentally friendly coatings for potential antifouling applications. *Phys. Chem. Chem. Phys.* **2016**, *18*, 7114–7123. [[CrossRef](#)] [[PubMed](#)]
25. Li, X.; Xing, Y.; Jiang, Y.; Ding, Y.; Li, W. Antimicrobial activities of ZnO powder-coated PVC film to inactivate food pathogens. *Int. J. Food Sci. Technol.* **2009**, *44*, 2161–2168. [[CrossRef](#)]
26. Qiu, H.; Hölken, I.; Gapeeva, A.; Filiz, V.; Adelung, R.; Baum, M. Development and Characterization of Mechanically Durable Silicone-Polythiourethane Composites Modified with Tetrapodal Shaped ZnO Particles for the Potential Application as Fouling-Release Coating in the Marine Sector. *Materials* **2018**, *11*, 2413. [[CrossRef](#)] [[PubMed](#)]
27. Qiu, H.; Gapeeva, A.; Hölken, I.; Kaps, S.; Adelung, R.; Baum, M. Preventing algae adhesion using lubricant-modified polydimethylsiloxane/polythiourethane nanocomposite. *Mater. Des.* **2022**, *214*, 110389. [[CrossRef](#)]
28. Feng, K.; Qiu, H.; Gapeeva, A.; Li, X.; Li, Y.; Kaps, S.; Mishra, Y.; Adelung, R.; Baum, M.; Yu, L. Indole-functionalized polythiourethane/tetrapodal shaped ZnO nanocomposites for eco-friendly marine biofouling control. *Prog. Org. Coatings* **2023**, *185*, 107939. [[CrossRef](#)]
29. Klemm, S.; Baum, M.; Qiu, H.; Nan, Z.; Cavalheiro, M.; Teixeira, M.C.; Tendero, C.; Gapeeva, A.; Adelung, R.; Dague, E.; et al. Development of Polythiourethane/ZnO-Based Anti-Fouling Materials and Evaluation of the Adhesion of *Staphylococcus aureus* and *Candida glabrata* Using Single-Cell Force Spectroscopy. *Nanomaterials* **2021**, *11*, 271. [[CrossRef](#)]
30. Dalsin, J.L.; Lin, L.; Tosatti, S.; Vörös, J.; Textor, M.; Messersmith, P.B. Protein resistance of titanium oxide surfaces modified by biologically inspired mPEG- DOPA. *Langmuir* **2005**, *21*, 640–646. [[CrossRef](#)]
31. Kenausis, G.L.; Vörös, J.; Elbert, D.L.; Huang, N.; Hofer, R.; Ruiz-Taylor, L.; Textor, M.; Hubbell, J.A.; Spencer, N.D. Poly(l-lysine)-g-Poly(ethylene glycol) Layers on Metal Oxide Surfaces: Attachment Mechanism and Effects of Polymer Architecture on Resistance to Protein Adsorption. *J. Phys. Chem. B* **2000**, *104*, 3298–3309. [[CrossRef](#)]
32. Perrino, C.; Lee, S.; Choi, S.W.; Maruyama, A.; Spencer, N.D. A Biomimetic Alternative to Poly(ethylene glycol) as an Antifouling Coating: Resistance to Nonspecific Protein Adsorption of Poly(l-lysine)-graft-dextran. *Langmuir* **2008**, *24*, 8850–8856. [[CrossRef](#)] [[PubMed](#)]
33. Tripathi, D.; Ray, P.; Singh, A.V.; Kishore, V.; Singh, S.L. Durability of Slippery Liquid-Infused Surfaces: Challenges and Advances. *Coatings* **2023**, *13*, 1095. [[CrossRef](#)]
34. Chelmowski, R.; Köster, S.D.; Kerstan, A.; Prekelt, A.; Grunwald, C.; Winkler, T.; Metzler-Nolte, N.; Terfort, A.; Wöll, C. Peptide-Based SAMs that Resist the Adsorption of Proteins. *J. Am. Chem. Soc.* **2008**, *130*, 14952–14953. [[CrossRef](#)] [[PubMed](#)]
35. Deng, L.; Mrksich, M.; Whitesides, G.M. Self-assembled monolayers of alkanethiolates presenting tri (propylene sulfoxide) groups resist the adsorption of protein. *J. Am. Chem. Soc.* **1996**, *118*, 5136–5137. [[CrossRef](#)]
36. Holmlin, R.E.; Chen, X.; Chapman, R.G.; Takayama, S.; Whitesides, G.M. Zwitterionic SAMs that resist nonspecific adsorption of protein from aqueous buffer. *Langmuir* **2001**, *17*, 2841–2850. [[CrossRef](#)] [[PubMed](#)]
37. Prime, K.L.; Whitesides, G.M. Self-assembled organic monolayers: Model systems for studying adsorption of proteins at surfaces. *Science* **1991**, *252*, 1164. [[CrossRef](#)] [[PubMed](#)]
38. Prime, K.L.; Whitesides, G.M. Adsorption of proteins onto surfaces containing end-attached oligo (ethylene oxide): A model system using self-assembled monolayers. *J. Am. Chem. Soc.* **1993**, *115*, 10714–10721. [[CrossRef](#)]
39. Alpay, P.; Uygun, D.A. Usage of immobilized papain for enzymatic hydrolysis of proteins. *J. Mol. Catal. B: Enzym.* **2015**, *111*, 56–63. [[CrossRef](#)]
40. Gogoi, D.; Barman, T.; Choudhury, B.; Khan, M.; Chaudhari, Y.; Dehingia, M.; Pal, A.R.; Bailung, H.; Chutia, J. Immobilization of trypsin on plasma prepared Ag/PPAni nanocomposite film for efficient digestion of protein. *Mater. Sci. Eng. C* **2014**, *43*, 237–242. [[CrossRef](#)]
41. Kim, Y.D.; Dordick, J.S.; Clark, D.S. Siloxane-based biocatalytic films and paints for use as reactive coatings. *Biotechnol. Bioeng.* **2001**, *72*, 475–482. [[CrossRef](#)] [[PubMed](#)]

42. Lee, J.; Lee, I.; Nam, J.; Hwang, D.S.; Yeon, K.M.; Kim, J. Immobilization and Stabilization of Acylase on Carboxylated Polyaniline Nanofibers for Highly Effective Antifouling Application via Quorum Quenching. *ACS Appl. Mater. Interfaces* **2017**, *9*, 15424. [[CrossRef](#)] [[PubMed](#)]
43. Yuan, S.; Wan, D.; Liang, B.; Pehkonen, S.O.; Ting, Y.P.; Neoh, K.G.; Kang, E.T. Lysozyme-Coupled Poly(poly(ethylene glycol) methacrylate)—Stainless Steel Hybrids and Their Antifouling and Antibacterial Surfaces. *Langmuir* **2011**, *27*, 2761–2774. [[CrossRef](#)] [[PubMed](#)]
44. Carniello, V.; Peterson, B.W.; van der Mei, H.C.; Busscher, H.J. Physico-chemistry from initial bacterial adhesion to surface-programmed biofilm growth. *Adv. Colloid Interface Sci.* **2018**, *261*, 1–14. [[CrossRef](#)] [[PubMed](#)]
45. Mercier-Bonin, M.; Ouazzani, K.; Schmitz, P.; Lorthois, S. Study of bioadhesion on a flat plate with a yeast/glass model system. *J. Colloid Interface Sci.* **2004**, *271*, 342–350. [[CrossRef](#)] [[PubMed](#)]
46. Nakanishi, K.; Sakiyama, T.; Imamura, K. On the adsorption of proteins on solid surfaces, a common but very complicated phenomenon. *J. Biosci. Bioeng.* **2001**, *91*, 233–244. [[CrossRef](#)] [[PubMed](#)]
47. Sharma, I.; Pattanayek, S.K. Effect of surface energy of solid surfaces on the micro- and macroscopic properties of adsorbed BSA and lysozyme. *Biophys. Chem.* **2017**, *226*, 14–22. [[CrossRef](#)] [[PubMed](#)]
48. Xu, L.C.; Siedlecki, C.A. Effects of surface wettability and contact time on protein adhesion to biomaterial surfaces. *Biomaterials* **2007**, *28*, 3273–3283. [[CrossRef](#)]
49. Zouaghi, S.; Six, T.; Nuns, N.; Simon, P.; Bellayer, S.; Moradi, S.; Hatzikiriakos, S.G.; André, C.; Delaplace, G.; Jimenez, M. Influence of stainless steel surface properties on whey protein fouling under industrial processing conditions. *J. Food Eng.* **2018**, *228*, 38–49. [[CrossRef](#)]
50. Coquet, L.; Cosette, P.; Junter, G.A.; Beucher, E.; Saiter, J.M.; Jouenne, T. Adhesion of *Yersinia ruckeri* to fish farm materials: Influence of cell and material surface properties. *Colloids Surfaces B Biointerfaces* **2002**, *26*, 373–378. [[CrossRef](#)]
51. Oh, Y.; Lee, N.; Jo, W.; Jung, W.; Lim, J. Effects of substrates on biofilm formation observed by atomic force microscopy. *Ultramicroscopy* **2009**, *109*, 874–880. [[CrossRef](#)] [[PubMed](#)]
52. Kalasin, S.; Dabkowski, J.; Nuesslein, K.; Santore, M.M. The role of nano-scale heterogeneous electrostatic interactions in initial bacterial adhesion from flow: A case study with *Staphylococcus Aureus*. *Colloids Surfaces B-Biointerfaces* **2010**, *76*, 489–495. [[CrossRef](#)] [[PubMed](#)]
53. Fukuzaki, S.; Urano, H.; Nagata, K. Adsorption of bovine serum albumin onto metal oxide surfaces. *J. Ferment. Bioeng.* **1996**, *81*, 163–167. [[CrossRef](#)]
54. Altankov, G.; Richau, K.; Groth, T. The role of surface zeta potential and substratum chemistry for regulation of dermal fibroblasts interaction. *Mater. Werkst.* **2003**, *34*, 1120–1128. [[CrossRef](#)]
55. Guillemot, G.; Lorthois, S.; Schmitz, P.; Mercier-Bonin, M. Evaluating the Adhesion Force Between *Saccharomyces Cerevisiae* Yeast Cells and Polystyrene From Shear-Flow Induced Detachment Experiments. *Chem. Eng. Res. Des.* **2007**, *85*, 800–807. [[CrossRef](#)]
56. Castelain, M.; Rouxhet, P.G.; Pignon, F.; Magnin, A.; Piau, J.M. Single-cell adhesion probed in-situ using optical tweezers: A case study with *Saccharomyces cerevisiae*. *J. Appl. Phys.* **2012**, *111*, 114701. [[CrossRef](#)]
57. Castelain, M.; Pignon, F.; Piau, J.M.; Magnin, A.; Mercier-Bonin, M.; Schmitz, P. Removal forces and adhesion properties of *Saccharomyces cerevisiae* on glass substrates probed by optical tweezer. *J. Chem. Phys.* **2007**, *127*, 135104. [[CrossRef](#)]
58. Talluri, S.N.L.; Winter, R.M.; Salem, D.R. Conditioning film formation and its influence on the initial adhesion and biofilm formation by a cyanobacterium on photobioreactor materials. *Biofouling* **2020**, *36*, 183–199. [[CrossRef](#)]
59. Lorite, G.S.; Rodrigues, C.M.; de Souza, A.A.; Kranz, C.; Mizaiikoff, B.; Cotta, M.A. The role of conditioning film formation and surface chemical changes on *Xylella fastidiosa* adhesion and biofilm evolution. *J. Colloid Interface Sci.* **2011**, *359*, 289–295. [[CrossRef](#)]
60. Jain, A.; Bhosle, N.B. Biochemical composition of the marine conditioning film: Implications for bacterial adhesion. *Biofouling* **2009**, *25*, 13–19. [[CrossRef](#)]
61. Garrido, K.D.; Palacios, R.J.S.; Lee, C.; Kang, S. Impact of conditioning film on the initial adhesion of *E. coli* on polysulfone ultrafiltration membrane. *J. Ind. Eng. Chem.* **2014**, *20*, 1438–1443. [[CrossRef](#)]
62. Hwang, G.; Kang, S.; El-Din, M.G.; Liu, Y. Impact of conditioning films on the initial adhesion of *Burkholderia cepacia*. *Colloids Surfaces B: Biointerfaces* **2012**, *91*, 181–188. [[CrossRef](#)] [[PubMed](#)]
63. Hwang, G.; Liang, J.; Kang, S.; Tong, M.; Liu, Y. The role of conditioning film formation in *Pseudomonas aeruginosa* PAO1 adhesion to inert surfaces in aquatic environments. *Biochem. Eng. J.* **2013**, *76*, 90–98. [[CrossRef](#)]
64. Kerchove, A.J.d.; Elimelech, M. Impact of Alginate Conditioning Film on Deposition Kinetics of Motile and Nonmotile *Pseudomonas aeruginosa* Strains. *Appl. Environ. Microbiol.* **2007**, *73*, 5227–5234. [[CrossRef](#)] [[PubMed](#)]
65. Démonstrateur API Qualité des Rivières Hub'Eau. Available online: <https://hubeau.eaufrance.fr/sites/default/files/api/demo/qualriv.htm> (accessed on 15 October 2023).
66. Triquet, T.; Tendero, C.; Latapie, L.; Manero, M.H.; Richard, R.; Andriantsiferana, C. TiO<sub>2</sub> MOCVD coating for photocatalytic degradation of ciprofloxacin using 365 nm UV LEDs - kinetics and mechanisms. *J. Environ. Chem. Eng.* **2020**, *8*, 104544. [[CrossRef](#)]
67. Etchepare, P.L.; Baggetto, L.; Vergnes, H.; Samélor, D.; Sadowski, D.; Caussat, B.; Vahlas, C. Process-structure-properties relationship in direct liquid injection chemical vapor deposition of amorphous alumina from aluminum tri-isopropoxide. *Phys. Status Solidi C* **2015**, *12*, 944–952. [[CrossRef](#)]

68. Santucci, V.; Maury, F.; Senocq, F. Vapor phase surface functionalization under ultra violet activation of parylene thin films grown by chemical vapor deposition. *Thin Solid Film.* **2010**, *518*, 1675–1681. [[CrossRef](#)]
69. Mercier-Bonin, M.; Adoue, M.; Zanna, S.; Marcus, P.; Combes, D.; Schmitz, P. Evaluation of adhesion force between functionalized microbeads and protein-coated stainless steel using shear-flow-induced detachment. *J. Colloid. Interface Sci.* **2009**, *338*, 73–81. [[CrossRef](#)]
70. Bousse, L.; Mostarshed, S.; Van Der Shoot, B.; de Rooij, N.F.; Gimmel, P.; Göpel, W. Zeta potential measurements of Ta<sub>2</sub>O<sub>5</sub> and SiO<sub>2</sub> thin films. *J. Colloid Interface Sci.* **1991**, *147*, 22–32. [[CrossRef](#)]
71. Roessler, S.; Zimmermann, R.; Scharnweber, D.; Werner, C.; Worch, H. Characterization of oxide layers on Ti<sub>6</sub>Al<sub>4</sub>V and titanium by streaming potential and streaming current measurements. *Colloids Surfaces B: Biointerfaces* **2002**, *26*, 387–395. [[CrossRef](#)]
72. Werner, C.; Korber, H.; Zimmermann, R.; Dukhin, S.; Jacobasch, H.J. Extended electrokinetic characterization of flat solid surfaces. *J. Colloid Interface Sci.* **1998**, *208*, 329–346. [[CrossRef](#)]
73. van Oss, C.J. *Interfacial Forces in Aqueous Media*; Taylor & Francis: Oxford, UK, 1994.
74. Wagner, C.D.; Naumkin, A.V.; Kraut-Vass, A.; Allison, J.W.; Powell, C.J.; Rumble, J.R., Jr. *NIST Standard Reference Database 20; Version 3.4 (Web Version)*; National Institute of Standards and Technology: Gaithersburg, MD, USA, 2003; p. 20899.
75. Castelain, M.; Duviau, M.P.; Oxaran, V.; Schmitz, P.; Coccain-Bousquet, M.; Loubiere, P.; Piard, J.C.; Mercier-Bonin, M. Oligomerized backbone pilin helps pilated *Lactococcus lactis* to withstand shear flow. *Biofouling* **2016**, *32*, 911–923. [[CrossRef](#)] [[PubMed](#)]
76. Jolliffe, I.T.; Cadima, J. Principal component analysis: A review and recent developments. *Philos. Trans. R. Soc. A: Math. Phys. Eng. Sci.* **2016**, *374*, 20150202. [[CrossRef](#)] [[PubMed](#)]
77. Biesinger, M.C.; Lau, L.W.M.; Gerson, A.R.; Smart, R.S.C. Resolving surface chemical states in XPS analysis of first row transition metals, oxides and hydroxides: Sc, Ti, V, Cu and Zn. *Appl. Surf. Sci.* **2010**, *257*, 887–898. [[CrossRef](#)]
78. Rouxhet, P.G.; Mozes, N.; Dengis, P.B.; Dufrêne, Y.F.; Gerin, P.A.; Genet, M.J. Application of X-ray photoelectron spectroscopy to microorganisms. *Colloids Surfaces B: Biointerfaces* **1994**, *2*, 347–369. [[CrossRef](#)]
79. Wang, C.; Zanna, S.; Frateur, I.; Despax, B.; Raynaud, P.; Mercier-Bonin, M.; Marcus, P. BSA adsorption on a plasma-deposited silver nanocomposite film controls silver release: A QCM and XPS-based modelling. *Surf. Coatings Technol.* **2016**, *307*, 1–8. [[CrossRef](#)]
80. Trantidou, T.; Payne, D.J.; Tsiligkiridis, V.; Chang, Y.C.; Toumazou, C.; Prodromakis, T. The dual role of Parylene C in chemical sensing: Acting as an encapsulant and as a sensing membrane for pH monitoring applications. *Sensors Actuators B Chem.* **2013**, *186*, 1–8. [[CrossRef](#)]
81. Frateur, I.; Lartundo-Rojas, L.; Méthivier, C.; Galtayries, A.; Marcus, P. Influence of bovine serum albumin in sulphuric acid aqueous solution on the corrosion and the passivation of an iron–chromium alloy. *Electrochim. Acta* **2006**, *51*, 1550–1557. [[CrossRef](#)]
82. Cai, K.; Frant, M.; Bossert, J.; Hildebrand, G.; Liefeth, K.; Jandt, K.D. Surface functionalized titanium thin films: Zeta-potential, protein adsorption and cell proliferation. *Colloids Surfaces B: Biointerfaces* **2006**, *50*, 1–8. [[CrossRef](#)]
83. Subramani, A.; Huang, X.; Hoek, E.M.V. Direct observation of bacterial deposition onto clean and organic-fouled polyamide membranes. *J. Colloid Interface Sci.* **2009**, *336*, 13–20. [[CrossRef](#)]
84. Beragoui, M.; Aguir, C.; Khalfaoui, M.; Enciso, E.; Torralvo, M.J.; Duclaux, L.; Reinert, L.; Vayer, M.; Ben Lamine, A. Bovine serum albumin adsorption onto functionalized polystyrene lattices: A theoretical modeling approach and error analysis. *Prog. Theor. Exp. Phys.* **2015**, *2015*, 033J01. [[CrossRef](#)]
85. Larsericsdotter, H.; Oscarsson, S.; Buijs, J. Structure, stability, and orientation of BSA adsorbed to silica. *J. Colloid Interface Sci.* **2005**, *289*, 26–35. [[CrossRef](#)] [[PubMed](#)]
86. Delivopoulos, E.; Ouberai, M.M.; Coffey, P.D.; Swann, M.J.; Shakesheff, K.M.; Welland, M.E. Serum protein layers on parylene-C and silicon oxide: Effect on cell adhesion. *Colloids Surfaces B Biointerfaces* **2015**, *126*, 169–177. [[CrossRef](#)] [[PubMed](#)]
87. Scarangella, A.; Soumbo, M.; Villeneuve-Faure, C.; Mlayah, A.; Bonafos, C.; Monje, M.C.; Roques, C.; Makasheva, K. Adsorption properties of BSA and DsRed proteins deposited on thin SiO<sub>2</sub> layers: Optically non-absorbing versus absorbing proteins. *Nanotechnology* **2018**, *29*, 115101. [[CrossRef](#)] [[PubMed](#)]
88. Crick, C.R.; Ismail, S.; Pratten, J.; Parkin, I.P. An investigation into bacterial attachment to an elastomeric superhydrophobic surface prepared via aerosol assisted deposition. *Thin Solid Film.* **2011**, *519*, 3722–3727. [[CrossRef](#)]
89. Privett, B.J.; Youn, J.; Hong, S.A.; Lee, J.; Han, J.; Shin, J.H.; Schoenfish, M.H. Antibacterial Fluorinated Silica Colloid Superhydrophobic Surfaces. *Langmuir* **2011**, *27*, 9597–9601. [[CrossRef](#)] [[PubMed](#)]
90. Tang, P.; Zhang, W.; Wang, Y.; Zhang, B.; Wang, H.; Lin, C.; Zhang, L. Effect of Superhydrophobic Surface of Titanium on *Staphylococcus aureus* Adhesion. *J. Nanomater.* **2011**, *2011*, 1–8. [[CrossRef](#)]
91. Friedlander, R.S.; Vlamakis, H.; Kim, P.; Khan, M.; Kolter, R.; Aizenberg, J. Bacterial flagella explore microscale hummocks and hollows to increase adhesion. *Proc. Natl. Acad. Sci.* **2013**, *110*, 5624–5629. [[CrossRef](#)]
92. Lu, N.; Zhang, W.; Weng, Y.; Chen, X.; Cheng, Y.; Zhou, P. Fabrication of PDMS surfaces with micro patterns and the effect of pattern sizes on bacteria adhesion. *Food Control* **2016**, *68*, 344–351. [[CrossRef](#)]
93. Thewes, N.; Loskill, P.; Jung, P.; Peisker, H.; Bischoff, M.; Herrmann, M.; Jacobs, K. Hydrophobic interaction governs unspecific adhesion of staphylococci: A single cell force spectroscopy study. *Beilstein J. Nanotechnol.* **2014**, *5*, 1501–1512. [[CrossRef](#)]
94. Castelain, M.; Pignon, F.; Piau, J.M.; Magnin, A. The initial single yeast cell adhesion on glass via optical trapping and Derjaguin-Landau-Verwey-Overbeek predictions. *J. Chem. Phys.* **2008**, *128*, 135101. [[CrossRef](#)] [[PubMed](#)]

95. Israelachvili, J. *Intermolecular and Surface Forces*; Elsevier: Amsterdam, The Netherlands, 2011. [[CrossRef](#)]
96. Rijnaarts, H.H.; Norde, W.; Lyklema, J.; Zehnder, A.J. DLVO and steric contributions to bacterial deposition in media of different ionic strengths. *Colloids Surfaces B: Biointerfaces* **1999**, *14*, 179–195. [[CrossRef](#)]
97. Vadillo-Rodríguez, V.; Busscher, H.J.; Mei, H.C.V.D.; Vries, J.D.; Norde, W. Role of lactobacillus cell surface hydrophobicity as probed by AFM in adhesion to surfaces at low and high ionic strength. *Colloids Surfaces B Biointerfaces* **2005**, *41*, 33–41. [[CrossRef](#)] [[PubMed](#)]
98. Gallardo-Moreno, A.; González-Martín, M.; Pérez-Giraldo, C.; Bruque, J.; Gómez-García, A. The measurement temperature: An important factor relating physicochemical and adhesive properties of yeast cells to biomaterials. *J. Colloid Interface Sci.* **2004**, *271*, 351–358. [[CrossRef](#)] [[PubMed](#)]
99. Brant, J. Assessing short-range membrane–colloid interactions using surface energetics. *J. Membr. Sci.* **2002**, *203*, 257–273. [[CrossRef](#)]
100. Millsap, K.W.; Bos, R.; Busscher, H.J.; Van Der Mei, H.C. Surface Aggregation of *Candida albicans* on Glass in the Absence and Presence of Adhering *Streptococcus gordonii* in a Parallel-Plate Flow Chamber: A Surface Thermodynamical Analysis Based on Acid–Base Interactions. *J. Colloid Interface Sci.* **1999**, *212*, 495–502. [[CrossRef](#)] [[PubMed](#)]
101. Kang, S.; Choi, H. Effect of surface hydrophobicity on the adhesion of *S. cerevisiae* onto modified surfaces by poly(styrene-ran-sulfonic acid) random copolymers. *Colloids Surfaces B Biointerfaces* **2005**, *46*, 70–77. [[CrossRef](#)]
102. Bos, R.; Busscher, H.J. Role of acid–base interactions on the adhesion of oral streptococci and actinomyces to hexadecane and chloroform—influence of divalent cations and comparison between free energies of partitioning and free energies obtained by extended DLVO analysis. *Colloids Surfaces B Biointerfaces* **1999**, *14*, 169–177. [[CrossRef](#)]
103. Dufrière, Y.F.; Boonaert, C.J.P.; Rouxhet, P.G. Surface analysis by X-ray photoelectron spectroscopy in study of bioadhesion and biofilms. In *Methods in Enzymology*; Academic Press: Cambridge, MA, USA, 1999; Volume 310, pp. 375–389. [[CrossRef](#)]
104. Dufrière, Y.F.; Boonaert, C.J.P.; Rouxhet, P.G. Adhesion of *Azospirillum brasilense*: Role of proteins at the cell-support interface. *Colloids Surfaces B Biointerfaces* **1996**, *7*, 113–128. [[CrossRef](#)]
105. Dewez, J.L.; Doren, A.; Schneider, Y.J.; Rouxhet, P.G. Competitive adsorption of proteins: Key of the relationship between substratum surface properties and adhesion of epithelial cells. *Biomaterials* **1999**, *20*, 547–559. [[CrossRef](#)]
106. Ercan, B.; Taylor, E.; Alpaslan, E.; Webster, T.J. Diameter of titanium nanotubes influences anti-bacterial efficacy. *Nanotechnology* **2011**, *22*, 295102. [[CrossRef](#)] [[PubMed](#)]
107. Ivanova, E.P.; Truong, V.K.; Wang, J.Y.; Berndt, C.C.; Jones, R.T.; Yusuf, I.I.; Peake, I.; Schmidt, H.W.; Fluke, C.; Barnes, D.; et al. Impact of Nanoscale Roughness of Titanium Thin Film Surfaces on Bacterial Retention. *Langmuir* **2010**, *26*, 1973–1982. [[CrossRef](#)] [[PubMed](#)]
108. Lüdecke, C.; Bossert, J.; Roth, M.; Jandt, K.D. Physical vapor deposited titanium thin films for biomedical applications: Reproducibility of nanoscale surface roughness and microbial adhesion properties. *Appl. Surf. Sci.* **2013**, *280*, 578–589. [[CrossRef](#)]
109. Desrousseaux, C.; Sautou, V.; Descamps, S.; Traoré, O. Modification of the surfaces of medical devices to prevent microbial adhesion and biofilm formation. *J. Hosp. Infect.* **2013**, *85*, 87–93. [[CrossRef](#)] [[PubMed](#)]
110. Yang, M.; Ding, Y.; Ge, X.; Leng, Y. Control of bacterial adhesion and growth on honeycomb-like patterned surfaces. *Colloids Surfaces B Biointerfaces* **2015**, *135*, 549–555. [[CrossRef](#)] [[PubMed](#)]
111. Vadillo-Rodríguez, V.; Guerra-García-Mora, A.I.; Perera-Costa, D.; González-Martín, M.L.; Fernández-Calderón, M.C. Bacterial response to spatially organized microtopographic surface patterns with nanometer scale roughness. *Colloids Surfaces B Biointerfaces* **2018**, *169*, 340–347. [[CrossRef](#)]

**Disclaimer/Publisher’s Note:** The statements, opinions and data contained in all publications are solely those of the individual author(s) and contributor(s) and not of MDPI and/or the editor(s). MDPI and/or the editor(s) disclaim responsibility for any injury to people or property resulting from any ideas, methods, instructions or products referred to in the content.